Geochemistry, Geophysics, Geosystems

RESEARCH ARTICLE
10.1029/2020GC009212

Trachytic Melt Inclusions Hosted in Clinopyroxene Offer a Glimpse Into Samoan EM2-Endmember Melts

J. V. Adams[1], F. J. Spera[1], and M. G. Jackson[1]

[1]Department of Earth Science, University of California Santa Barbara, Santa Barbara, CA, USA

Key Points:

- Reconstructed clinopyroxene-hosted melt inclusions from an enriched (high $^{87}Sr/^{86}Sr$) Samoa hot spot lava are trachytic
- Melt inclusion chemical variability is not the result of post-entrapment crystallization or diffusion, but represents magma heterogeneity upon capture
- The melt inclusions are a mixing endmember for a suite of enriched Samoan lavas and may be evidence of Enriched Mantle two derived liquids

Supporting Information:

- Supporting Information S1
- Data Set S1
- Data Set S2
- Data Set S3
- Data Set S4
- Data Set S5
- Data Set S6

Correspondence to:
J. V. Adams,
adams@ucsb.edu

Citation:
Adams, J. V., Spera, F. J., & Jackson, M. G. (2021). Trachytic melt inclusions hosted in clinopyroxene offer a glimpse into Samoan EM2-endmember melts. *Geochemistry, Geophysics, Geosystems*, *22*, e2020GC009212. https://doi.org/10.1029/2020GC009212

Received 1 JUN 2020
Accepted 20 JAN 2021

Abstract We present major and trace element data on clinopyroxene-hosted, glassy melt inclusions (MIs) from a highly enriched (high $^{87}Sr/^{86}Sr = 0.71856$) lava (ALIA-D115-18) from the Samoan hot spot. Following correction for post-entrapment crystallization, the MIs are trachytic (62.6–65.4 wt% SiO_2, 1.5–3.0 wt% MgO, and 7.2–10.6 wt% total alkalis ($Na_2O + K_2O$)) ALIA-D115 lavas dredged off the submarine flanks of Savai'i Island, western Samoa have previously been suggested to exhibit binary endmember magma mixing between a mafic, low $^{87}Sr/^{86}Sr$ magma and an evolved, high $^{87}Sr/^{86}Sr$ magma (the Enriched Mantle 2 endmember; EM2). In major and trace element space, these ALIA-D115 lavas form a mixing trend between more primitive Samoan shield lavas and the MIs of this study, suggesting the MIs could represent the EM2-derived mixing endmember. Recent efforts to constrain the EM2 mixing endmember composition shows remarkable overlap with the MI compositions, supporting the argument they could represent the $^{87}Sr/^{86}Sr$ mixing endmember to the ALIA-D115 lavas and are derived from the EM2 endmember. Additionally, one melt inclusion contains Fo_{73} olivines not in equilibrium with the trachytic melt, suggesting the melt interacted with a mafic magma prior to entrapment within host clinopyroxene. Projecting the ALIA-D115 mixing trend in $^{87}Sr/^{86}Sr$ versus SiO_2 and K_2O space shows that the trend intersects an average MI composition at $^{87}Sr/^{86}Sr$ values of ~0.725, thereby offering a window into more extreme compositions associated with the EM2 endmember.

Plain Language Summary Droplets of silicate melt (i.e. melt inclusions) captured in the mineral clinopyroxene were measured for their chemistry. The melt inclusions and their clinopyroxene hosts are found in one lava recovered from the submarine flanks of Savai'i Island—an oceanic island formed along the Samoan hot spot track. The melt compositions represent silicate liquids present during magma evolution beneath Samoa. Lavas erupted at Samoa uniquely show extreme chemical signatures associated with ancient continentally derived sediment that has been recycled into Earth's interior via subduction. These diagnostic recycled materials have subsequently been incorporated into the Samoan plume, although the composition and origin of this material remains enigmatic. The melt inclusions provide a window into the composition of this recycled material and this study shows the melt inclusions may have been derived from a sediment-infiltrated source. Remarkably, mixing between the melt inclusions and other compositionally distinct lavas from Samoa can explain the range in chemistry of lavas dredged from Savai'i Island. The Samoan melt inclusions help us understand the origin and evolution of the source contributing to the volcanic rocks of the Samoan hotspot, and ultimately, the chemical evolution of the Earth's mantle.

1. Introduction

Melt inclusions (MIs) have been used for decades to provide a glimpse into the petrogenetic evolution of lavas (e.g., Anderson & Wright, 1972; Danyushevsky et al., 2002; Kent, 2008; Kent & Elliott, 2002; Lowenstern, 1995; Melson, 1983; Plank et al., 2013; Sobolev, 1996). Melt inclusions represent liquids present in evolving magmas captured by growing phenocrysts and can be used to better understand the evolution of a magma. Conceptually, these captured melts are physically isolated from the effects of subsequent (post-entrapment) magma mixing, assimilation, or fractionation that ultimately modify magma compositions. They present compositional snapshots in time, although following entrapment MI compositions may be modified by post-entrapment crystallization (PEC) or by post-entrapment diffusive exchange (PED) with their host crystal. MIs often reveal highly heterogenous compositions, or distinct compositions not realized by the associated erupted products (e.g., Kamenetsky, 1996; Kamenetsky et al., 1997; Kent et al., 1999;

Maclennan, 2008; Reinhard et al., 2018; Rowe et al., 2011; Saal et al., 1998; Sobolev et al., 2000; Sobolev & Shimizu, 1993; Sours-Page et al., 1999; Wallace, 2005). Compared with the whole rock, these differences in composition are likely a direct result of sampling different time frames during melting and mixing processes, or even different mantle sources than are present in whole rock lavas (e.g., Jackson & Hart, 2006; Saal et al., 1998; Sobolev, 2007). Other work suggests anomalous melt inclusion compositions could also be the result of dissolution-reaction-mixing processes at the grain-scale within the magma chamber due to injections of new magma that results in partial dissolution of mush zones (Danyushevsky et al., 2004). In either case, melt inclusions can be used to help better understand lava petrogenesis.

Here, we focus on reconstructed major and trace element compositions of uniformly trachytic clinopyroxene-hosted melt inclusions found within the second-most-enriched (high $^{87}Sr/^{86}Sr = 0.71856$) whole rock lava from the Samoa hot spot (whole-rock chemistry can be found in Jackson et al., 2007). This lava, ALIA-D115-18, was dredged off the submarine flanks of Savai'i Island, western Samoa, and similar to other lavas from the same dredge haul—(ALIA115 dredge haul) showing the most geochemically enriched $^{87}Sr/^{86}Sr$ values ever measured in relatively fresh whole rock ocean island basalts (OIB)—this lava exhibits the "enriched mantle 2" (EM2) geochemical signature (Jackson et al., 2007). The EM2 signature is believed to be the result of addition of ancient subducted terrigenous sediment to the mantle source region (Adams et al., 2021; Edwards et al., 2019; Jackson et al., 2007; White & Hofmann, 1982). However, important questions remain regarding the composition of EM2 or its source, including the precise composition of the EM2 endmember, the petrogenetic history of EM2-derived OIB melts, and how these melts mix with non-EM2 melts in magma chambers. A recent study by Adams et al. (2021) uses binary mixing theory, high precision $^{87}Sr/^{86}Sr$ and $^{143}Nd/^{144}Nd$ analyses of single-crystal magmatic clinopyroxene, and major and trace element data of clinopyroxenes within the ALIA-D115-18 sample to calculate the EM2 magma mixing endmember as being trachytic in composition. Further, this trachytic composition is shown to represent a magma mixing endmember, that when mixed with a much more mafic endmember, can reproduce the chemical signatures observed in the entire ALIA-D115 lava suite from which ALIA-D115-18 is derived. The work presented here uses the clinopyroxene-hosted melt inclusions in the ALIA-D115-18 sample to place further constraints on the composition and petrogenetic history of EM2. We emphasize that, remarkably, the range of calculated trachytic EM2 endmember model melts from Adams et al. (2021) bear a striking resemblance to the trachytic melt inclusions of this study.

We suggest below that the clinopyroxene-hosted trachytic MIs in sample ALIA-D115-18, once corrected for post-entrapment crystallization, are EM2-endmember melts captured during the magma mixing process. One clinopyroxene-hosted MI has two partially resorbed Fo_{73} olivine crystals, suggesting interaction of the trachytic melt with a mafic magma as the olivines and the surrounding trachyte melt are not in equilibrium. This observation is consistent with two-component mixing between a mafic (olivine-bearing) magma and a much more evolved magma that has been inferred from relationships between major and trace element compositions and radiogenic isotopic ratios in the Samoan magmatic suite alluded to above (Adams et al., 2021; Edwards et al., 2019; Jackson et al., 2007). This raises several important questions: what is the origin of these high-silica MIs? What is their relationship to the ALIA-D115-18 whole rock and the EM2 source? Once corrected for possible post-entrapment modification, do they represent relatively primary high-silica partial melts that were trapped in growing clinopyroxenes at depth during magma mixing? These questions are addressed in the following sections.

2. Samples and Methods

Melt inclusions of this study are hosted in clinopyroxenes from a single Samoan hotspot lava (ALIA-D115-18), dredged off the submarine flanks of Savai'i Island, western Samoa. Twenty-two MIs were studied with diameters ranging from ~15 to 100 μm. The MIs are generally spherical or ellipsoidal in cross-section and are mostly glassy; some contain minor amounts of crystal inclusions consisting of clinopyroxene ~ ilmenite >> olivine (Figure 1). Of the 22 inclusions, vapor bubbles are observed in two MIs occupying between 11 and 26 vol% of the MI volume, one shows significant amounts of crystal inclusions representing ~10 vol% of the MI (Figure 1a), one has ~2 vol% of ilmenite (Figure 1b), and, most significantly, 20 MIs (91%) show <2 vol% of crystal inclusions. The crystal volume estimate was made assuming an ellipsoidal geometry for both the MI and the crystals.

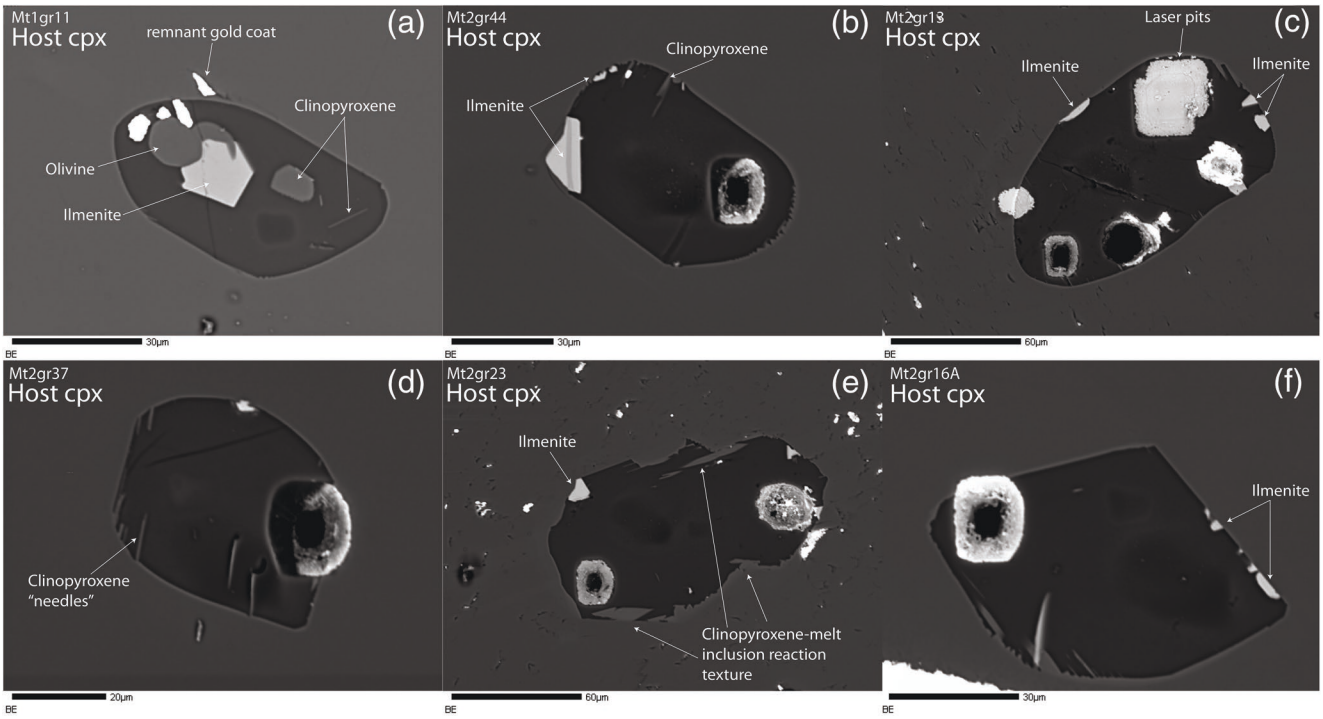

Figure 1. Back-scatter electron (BSE) images of select melt inclusions. (a) Melt inclusion with the largest amount and variety of crystal inclusions. (b) and (c) are relatively pristine melt inclusions with some ilmenite crystal inclusions nucleating on the melt inclusion walls. (d) Relatively pristine melt inclusion showing clinopyroxene needles that have nucleated in the inclusion (e) one of two melt inclusions that show direct reaction of the melt inclusion walls with the surrounding clinopyroxene. The reaction texture is denoted by the jagged appearance of the melt inclusion wall. In addition, there is a slightly brighter region around the melt inclusion edge compared with the rest of the host clinopyroxene, indicative of compositionally distinct clinopyroxene. (f) Melt inclusions showing minimal daughter crystals. All of the above melt inclusions also show laser and ion probe pits, and remnant gold coat in regions of low topography is visible as bright regions in the images. See Supporting Figure S10 for BSE images of the other melt inclusions analyzed in this study.

For volatile and trace element analysis of the melt inclusions by ion probe, the sample surface was pre-sputtered prior to analysis. Volatile (H_2O, Cl, F, and S) elements in the melt inclusions were analyzed on the Cameca IMS 6F ion microprobe housed at the Department of Terrestrial Magnetism (DTM), Carnegie Institution of Washington following methods from Hauri (2002), where uncertainties are ± 10% (2σ) for volatile element concentrations. Trace element (Sc, Sr, Nd, Y, Zr, Ba, Ce, Dy, Nb, La, Yb, Hf, and Gd) analyses of the glassy portions of the melt inclusions were also carried out on the DTM Cameca IMS 6F and following techniques in Peterson et al. (2017), where precision on trace element analyses is better than 10% (2σ). Secondary standard ALV 519-4-1 was measured along with the melt inclusion trace element measurements. These measurements can be found in Data Set S1. Major element concentrations in the melt inclusions were measured on the JEOL Superprobe housed at the Geophysical Laboratory, Carnegie Institution of Washington, and methods and uncertainties follow Hauri (2002): a 15 kV accelerating voltage was used, and a 10 nA, defocused (10 µm) beam was employed during analysis. Lastly, it is important to note these melt inclusions were never heated (e.g., by heating stage or furnace) for rehomogenization. New major, trace, and volatile element data on melt inclusions are shown in Data Set S2.

Major element concentrations in the hosting clinopyroxenes and the olivine inclusions in the mt1gr11 MI (Data Set S2) were also measured on the JEOL Superprobe housed at the Geophysical Laboratory, Carnegie Institution of Washington, and methods and uncertainties follow Hauri (2002). Trace elements were measured in the host clinopyroxenes (Data Set S2) by LA-ICP-MS at the University of California Santa Barbara (UCSB) using a Photon Machines Excite 193 Excimer laser coupled to an Agilent 7700 quadrupole ICPMS. A 15 µm spot size was used and the reference material NIST612 was analyzed every 8–10 unknown analyses; analyses and the 2RSD on each element can be found in Data Set S3. Each trace element measurement reported in Data Set S2 is an average of three to four spot analyses spread across each clinopyroxene grain. Additionally, we measured 17 compositional profiles in four of the clinopyroxenes hosting melt inclusions

and the major and trace element data can be found in upporting Data Sets S4 and S5, respectively. Major and trace element analyses were carried out in several transects across four clinopyroxenes, extending from near the clinopyroxene-melt inclusion boundary to distal regions of the clinopyroxene, and analyses were carried out at UCSB. Major elements were analyzed on the EPMA at UCSB; an accelerating voltage of 15 kV was used with a 20 nA beam with a spot size of 2 μm.

Correction for PEC was performed on each individual MI. For each MI, 2% increments of the host clinopyroxene composition (for major, trace, and volatile elements—assuming zero concentration in the clinopyroxene for the volatiles, as volatiles were not measured in the clinopyroxenes) was added back into each MI bulk composition until the MI was saturated in clinopyroxene of Mg# matching the respective host composition Mg#. This iterative calculation was performed using the MELTS modeling software (Ghiorso & Sack, 1995; Gualda et al., 2012; the most applicable modeling software available for igneous phase equilibria calculations) in which, after each incremental addition of host clinopyroxene to the MI, the new bulk MI composition was input into MELTS to calculate the stable mineral assemblage from the liquidus to ~100°C below the liquidus. Once the calculated liquidus phase was clinopyroxene with a Mg# matching that of the real host clinopyroxene value, the process of clinopyroxene addition into the MI was complete. In the MELTS calculations, we used the Quartz-Magnetite-Fayalite oxygen buffer to dictate the ferrous to ferric Fe ratio—all Fe was converted back to ferrous Fe at the end of the calculation and thus, only total FeO is reported in Data Set S6. We tested a range of pressures for each calculation and results showed that the temperature of clinopyroxene saturation and the Mg# of that clinopyroxene for a given bulk composition were insensitive to pressure (i.e., the clinopyroxene saturation temperature and Mg# were within typical analytical uncertainties at a range of pressures). Although there are other daughter crystals within some of the MIs, the amount of clinopyroxene added back into the MIs far outweighs the volume percentage of other crystals, such as ilmenite (which may not all be daughter crystals, see below), so other daughter crystals were neglected from the reconstruction calculation. The original melt inclusion compositions and host clinopyroxene data can be found in Data Set S2. The reconstructed MI compositions and the amount of clinopyroxene addition to the MI to account for PEC can be found in Data Set S6.

3. Results

3.1. Major and Trace Elements

The original melt inclusions of this study were corrected for minor amounts of post-entrapment crystallization of the host clinopyroxene. The amount of clinopyroxene added back into the original melt inclusions ranges from 16% to 24% by mass, with most requiring less than 20%. The original measured and reconstructed melt inclusions are trachytic and show limited variability in the major elements with the exception of silica, Na_2O, and K_2O. The reconstructed melt inclusions lie between ~62.6–65.4 wt% SiO_2, 1.5–3.0 wt% MgO, and 7.2–10.6 wt% total alkalis ($Na_2O + K_2O$) (see Data Set S6 for full compositions).

Trace elements have been measured in 16 of the 22 inclusions. The reconstructed incompatible trace element compositions show much more variability compared with major elements (see Data Set S6 for major and trace element compositions). There is significant variability in the REEs, as can be seen in Figure 2, that is not explained by PEC (as discussed in the following section). A comparison of the melt inclusions with the ALIA-D115-18 whole rock and average Ta'u and Ofu lavas, which represent the least geochemically enriched lavas from Samoa, shows that most of the ALIA-D115-18 MIs are more enriched in Ba, Nb, K, and some light rare-earth elements (LREEs), and depleted in Ti and some heavy rare-earth elements (HREEs), compared with other Samoan whole rock lavas (Figure 2). Nb and Ti show distinct depletions for all of the MIs, likely related to ilmenite removal from the melt pre- or post-entrapment. Additionally, many of the MIs show positive or slight negative Sr anomalies (where Sr anomaly refers to the deviation of Sr above or below bracketing elements with similar incompatibility in a primitive mantle normalized spider diagram).

3.2. Volatiles

Water, sulfur, and the halogens have been measured in 18 of the 22 MIs. The original uncorrected MI compositions show H_2O contents ranging from 0.4 to 1.1 wt%, S ranging from 67 to 504 ppm, Cl ranging from 781 to 2916 ppm, and F ranging from 19 to 2674 ppm. Although the MI volatile elements were not analyzed

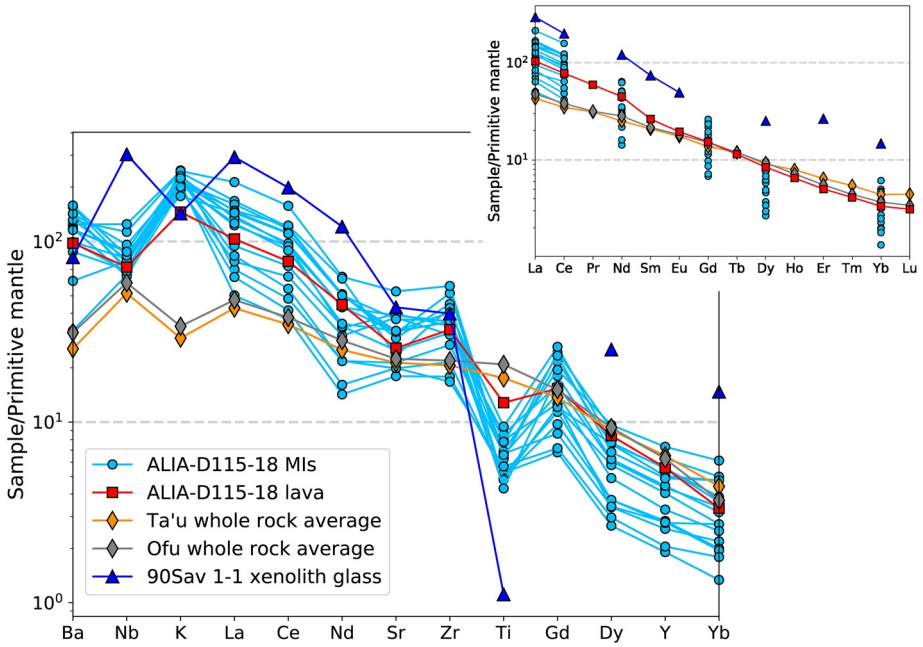

Figure 2. Primitive mantle normalize trace element patterns of clinopyroxene-hosted melt inclusions (MIs) (blue circles) from the ALIA-D115-18 whole rock lava (red squares; Jackson et al., 2007). The data are shown in comparison with other Samoa whole rocks that have geochemically depleted $^{87}Sr/^{86}Sr$ compositions (average compositions for Ta'u and Ofu whole rocks; samples with <7wt% MgO have been excluded). The orange and gray diamonds represent average Samoan lava compositions from Ta'u and Ofu Islands, respectively, which are the most geochemically depleted shield volcanoes in the eastern Samoan region. The dark blue triangles are a high silica, high $^{87}Sr/^{86}Sr$ (0.71234) Savai'i xenolith glass, 90SAV1-1, from Hauri et al. (1993). The inset spiderdiagram shows rare earth elements only. All of the MIs plotted are the reconstructed MIs from Data Set S6.

in the host clinopyroxene, important for making the correction for PEC, we simply assume the host clinopyroxenes have concentrations of 0 ppm for all volatiles (a valid assumption considering volatiles are highly incompatible in clinopyroxene) to make the PEC correction. The reconstructed volatile ranges are 0.3–0.9 wt% H_2O, 56–418 ppm S, 648–2449 ppm Cl, and 16–2219 ppm F (see Data Set S6). A comparison of any reconstructed volatile element with melt inclusion size shows no correlation, suggesting the variation in volatile concentrations, and in particular H_2O, has not been affected by diffusive loss (Cabral et al., 2014; Kent, 2008). F concentrations are highly variable across the MI suite. In the H_2O, Cl, and S dataset, one MI has anomalously low volatile concentrations compared with the rest of the MIs, and this inclusion is also the MI that shows the most faceted shape (Mt2gr16A; Figure 1f). We do not have an explanation for the low volatile concentrations in this inclusion, except to suggest that the inclusion may have ruptured during ascent, allowing some volatile loss, prior to reannealing.

4. Discussion

4.1. Post-entrapment Modification

Modification processes affecting MIs post-entrapment have been studied extensively by many authors (Baker, 2008; Bucholz et al., 2013; Cottrell et al., 2002; Danyushevsky et al., 2000, 2002; Gaetani et al., 2012; Gaetani & Watson, 2000, 2002; Kent, 2008; Kress & Ghiorso, 2004; Nielsen et al., 1998; Portnyagin et al., 2008; Qin et al., 1992; Schiano & Bourdon, 1999; Sobolev, 1996; Spandler et al., 2007). The two main ways in which MIs can be chemically modified post-entrapment are by: (1) nucleation and growth of the host mineral on the MI walls by reaction between the edge of the melt inclusion and host clinopyroxene, or nucleation and growth of phases within the MI that are different than the host mineral, and (2) diffusive re-equilibration of the MI with the host crystal. These modification processes and their effects on the MIs of this study are evaluated below.

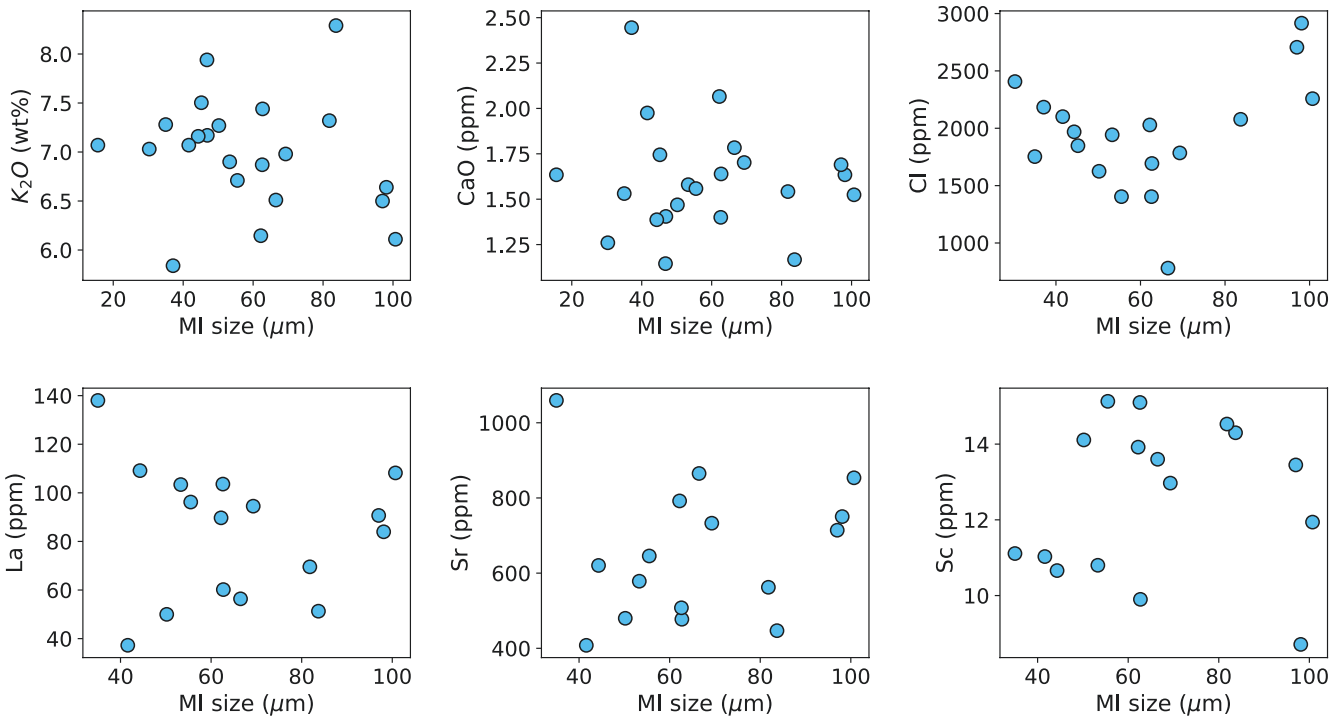

Figure 3. Melt inclusion size versus composition. If diffusive modification has played a significant role in modifying melt inclusion chemistry, a linear trend will be observed when comparing melt inclusion incompatible elements and size, as smaller inclusions will be affected more rapidly by diffusion compared with larger inclusions. Melt inclusion sizes and reconstructed compositions can be found in Data Sets S2 and S6, respectively.

4.1.1. Diffusive Modification

If diffusive re-equilibration has played an important role in modifying the melt inclusion compositions, we might expect a correlation between MI size and composition, with the smallest inclusions closest to equilibrium due to greater diffusive equilibration compared with large melt inclusions (e.g., Baker, 2008; Cottrell et al., 2002; Nielsen et al., 1998; Qin et al., 1992; Sinton et al., 1993). Of course, this is dependent on the fact that the MIs have not reached equilibrium among all inclusions, which in turn is dependent on magmatic residence times. Magmatic residence time calculations, based on Fe/Mg inter-diffusion within clinopyroxenes from the ALIA-D115-18 lava, show residence times about on the order of <100 years from clinopyroxene crystallization to eruption (Adams et al., 2021). This rather short residence time is insufficient to allow incompatible and most major elements in the MIs to fully re-equilibrate with their host based on diffusion calculations. To elucidate this fact, Figure 3 shows a series of plots of melt inclusion size versus composition for selected major and trace elements, for several incompatible (e.g., K_2O, Cl, La, and Sr) and two compatible (e.g., CaO and Sc) elements (or element oxides) in clinopyroxene. These plots show no clear correlations. Additional comparisons (not shown) of other chemical species, including both major and trace elements, also show a lack of correlation with melt inclusion size. This is consistent with the argument that magmatic residence times were very short and thus, PED of the melt inclusions has been negligible.

Additionally, boundary-layer driven diffusion can also be assessed as a means of modifying MI composition using a simple test of plotting element diffusivity in melt versus trace element standard deviation measured using the composition of all 22 MIs (Kent, 2008; Michael et al., 2002). Accordingly, fast diffusing elements should show little variation (low standard deviation) because diffusion will rapidly reduce ("smooth out") trace element variability in the clinopyroxene, while slow diffusing elements should show the most variability (high standard deviation). We test this in Figure S11 with a comparison of compositional standard deviation versus known diffusivities in trachytic melts at 1150°C for MI trace elements, and we observe no distinct correlations. This also supports the hypothesis that diffusion has played a negligible role in modifying the MIs and supports previous work from Adams et al. (2021) that magmatic residence times were too short for diffusion to have modified the bulk composition of the melt inclusions significantly.

4.1.2. Post-entrapment Crystallization

Of the melt inclusions presented in this study, 20 out of 22 show 2 vol% or less crystallinity. The crystal volume estimate was made assuming an ellipsoidal geometry for both the MI and the crystals. Of the 20 MIs with 2 vol% crystallinity or less, two show <<1 vol% crystal inclusions, but contain vapor bubbles. These two MIs (mt2gr9 and mt2gr8b; Figures S10i and S10h, respectively) are also the only two MIs that are surrounded by clinopyroxene "halos," which are rings of clinopyroxene—ranging from ~10 to 30 μm and encircle the MIs—with distinct mean atomic number observed only in back-scatter electron (BSE) imaging. These halos could be related to PEC. Compositional gradients in the clinopyroxenes going away from the MIs, including clinopyroxenes hosting halos (discussed in Text S1 and denoted by a gray dashed line in Figures S3 and S4), do show some evidence of compositional variability related to PEC. However, those inclusions that do show gradients consistent with PEC have very similar major element chemistry to those that do not show evidence of PEC, suggesting PEC is not the *primary* process for generation of trachytic compositions in the MIs, but we do acknowledge that PEC has occurred. Two MIs obviously exhibit evidence of PEC at the inclusion-clinopyroxene boundary: in one inclusion, this resulted in formation of orthopyroxene (melt inclusion Mt1gr12; see Figure S10e), and in another inclusion, the result is a jagged MI rim surrounded by compositionally distinct clinopyroxene (indicated by the brighter regions surrounding the MI in the BSE image—not to be confused with the previously descrived "halos" which are much larger and completely surround the MI—compared with the slightly darker host clinopyroxene) that returns to the host clinopyroxene composition with distance from the MI edge into the clinopyroxene (Mt2gr23; see Figure 1e).

Of the two MIs that show greater than 2 vol% crystallinity, one shows about 2.5 vol% of predominantly ilmenite (Mt2gr44: Figure 1b). The second of the two MIs with >2 vol% crystallinity (Mt1gr11; Figure 1a) contains crystals of Fo_{73} olivine + ilmenite + clinopyroxene representing a crystallinity of ~10 vol% of the MI. However, we argue these were not crystallized directly from the melt inclusion post-entrapment, but rather were trapped along with the melt simultaneously. In this single MI that exhibits the olivine, ilmenite, and clinopyroxene, the crystals *appear* isolated within the bulk volume of the MI and apparently have not grown from the MI walls. Observing the MI in 3D would help determine if the apparent isolation is definitive (e.g. Kent, 2008; Kress & Ghiorso, 2004; Roedder, 1984; Sobolev, 1996). However, perhaps more significantly, if these crystals *did* precipitate directly from the melt inclusion following entrapment, one expects that the MI would significantly differ in major element composition compared to other melt inclusions with little or no daughter crystals; this is not the case. Furthermore, the presence of Fo_{73} olivine in the trachytic melt inclusion provides further evidence that the olivine did not grow post-entrapment, as the olivine is out of equilibrium with the trachytic melt (and thus, the hosting clinopyroxene) according to the MELTS MI reconstruction calculations, which found no stable olivine in the equilibrium assemblage at a range of pressures, temperatures, and water concentrations tested. Additionally, no olivine phenocrysts exist in the ALIA-D115-18 whole rock, suggesting olivine was not crystallizing from the magma that gave rise to this sample, and further, the olivines are similar in composition to the range of olivine compositions found in forsteritic olivines in other more primitive Samoan shield lavas (see Jackson & Shirey, 2011). Lastly, the olivine and ilmenite within this inclusion appear visually to be intergrown suggesting *both* the ilmenite and olivine were trapped together and did not grow from this MI. To summarize, all but two MIs show much less than 2 vol% crystallinity with two showing 2–10 vol%. We argue that some of the crystals in the MIs are not related to PEC but were instead present at the time of magma mixing and MI entrapment.

Nevertheless, based on the reasoning above, it is clear that some PEC has occurred. This is perhaps most apparent in the fact that the original melt inclusions are not in equilibrium with their host-clinopyroxenes. Approximately 14%–24 % addition of clinopyroxene back into the "raw" MIs was needed to bring them into equilibrium with their host clinopyroxene (see Data Set S6 for exact values). However, again, given the reasoning above, we argue that the primary process controlling the compositional variability observed in the MIs is not PEC. The reconstructed compositions can be seen (in addition to the measured MI compositions) in Figures 4 and 5 and Data Set S6.

4.2. Origin of Trachytic Melt Inclusions

Several recent studies have shown the ALIA-D115 lavas—a suite of lavas from the same submarine dredge of a Samoan volcano (Savai'i) as the ALIA-D115-18 lava studied here—to be a result of magma mixing between

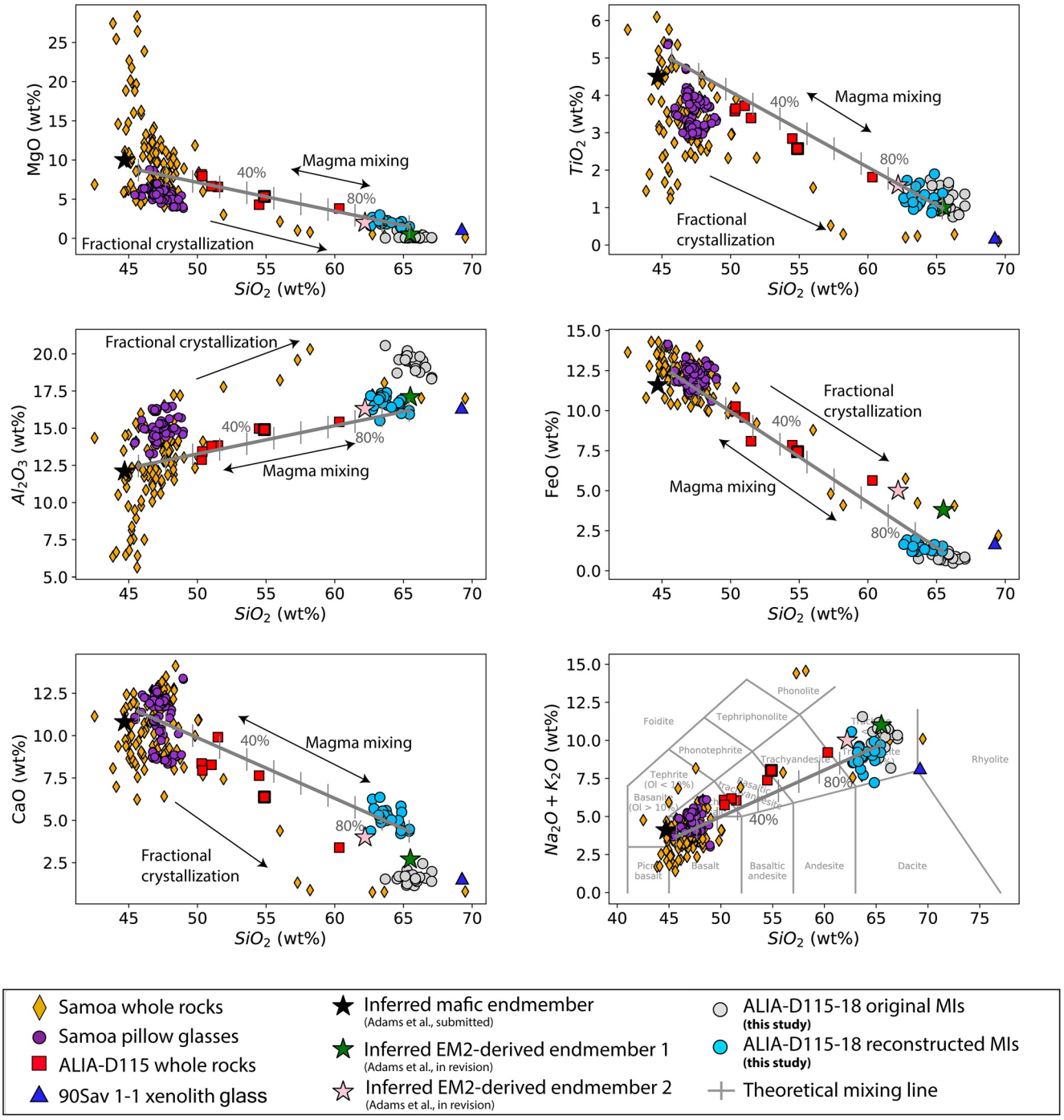

Figure 4. Major elements versus SiO_2 showing the relationship between the ALIA-D115 lavas (red squares; data from Jackson et al., 2007; the ALIA-D115-18 sample is outlined in bold), other Samoan whole rock lavas (orange diamonds), Samoan pillow glasses (purple circles), and the reconstructed ALIA-D115-18 melt inclusions (blue circles). Also plotted for reference are the original MI compositions (grey circles) in addition to the inferred mafic (black star) and inferred silicic (low MgO silicic EM2 melt endmember 1 = green star, high MgO silicic EM2 melt endmember 2 = pink star) mixing endmembers calculated by Adams et al. (2021). The high silica (trachytic), high-$^{87}Sr/^{86}Sr$ Savai'i xenolith glass from Hauri et al. (1993) is also shown for reference as a dark blue triangle. The ALIA-D115 lavas show a mixing trend extending from more primitive Samoan lavas and pillow glasses to the melt inclusions suggesting the melt inclusions could be a mixing endmember. The rest of the Samoan lavas (orange diamonds) that are more evolved show fractional crystallization trends. In addition, a mixing line (gray hatched line) has been calculated using a melt inclusion (mt2gr21; SiO_2 = 65.4 wt%, TiO_2 = 0.98 wt%, Al_2O_3 = 16.2 wt%, FeO = 1.2 wt%, MgO = 1.5 wt%, CaO = 4.4 wt%, and $Na_2O + K_2O$ = 9.7 wt%) and a primitive Samoan whole rock lava composition (OFU-04-05; SiO_2 = 45.7 wt%, TiO_2 = 5.0 wt%, Al_2O_3 = 12.5 wt%, FeO = 12.4 wt%, MgO = 8.7 wt%, CaO = 11.4 wt%, and $Na_2O + K_2O$ = 3.7 wt%) (Hart & Jackson, 2014) as endmembers. The mixing line captures the ALIA-D115 lavas quite well. The contribution of a trachytic MI composition to the mixture that is required to generate the most radiogenic (highest $^{87}Sr/^{86}Sr$) ALIA-D115 lava is about 70%–80%, consistent with that proposed by Adams et al. (2021).

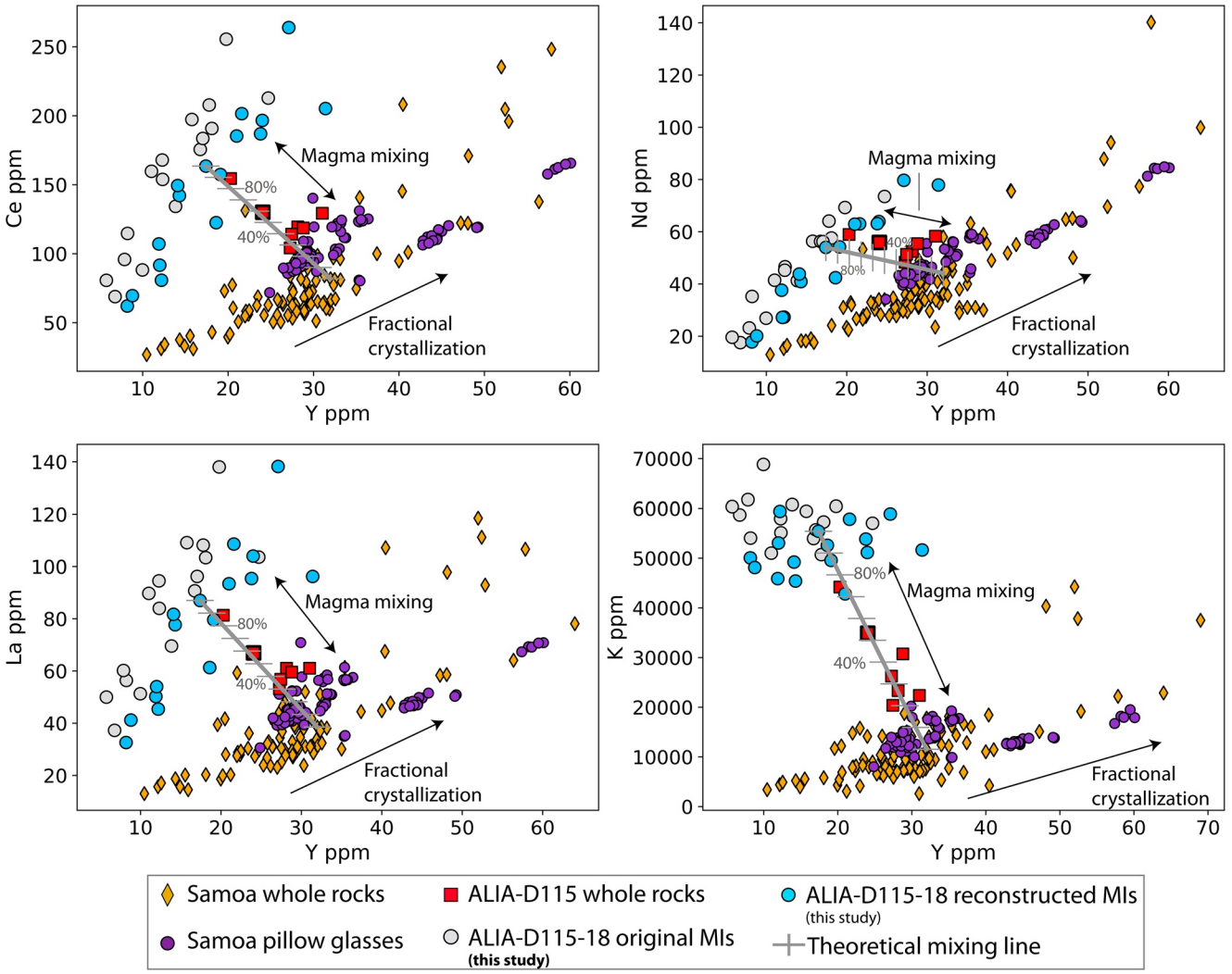

Figure 5. Select trace element plots comparing the ALIA-D115 lavas (red squares; data from Jackson et al., 2007; the ALIA-D115-18 sample is outlined in bold), other Samoan whole rock lavas (orange diamonds), Samoan pillow glasses (purple circles) and the ALIA-D115-18 melt inclusions (blue circles). Trace element data show the ALIA-D115 mixing trend is very clearly extending between more primitive Samoan whole rock lavas (or glasses) and the trend of the MIs of this study. The Samoa whole rock lavas show a clear fractional crystallization trend (positive slope) while the ALIA-D115 lavas form an orthogonal trend (negative slope) extending toward the MIs. Using the same two mixing endmembers as in Figure 4: the mt2gr21 melt inclusion (Y = 17.4, La = 87.0, Nd = 54.0, Ce = 163.5, K = 55,417) and a primitive Samoan whole rock lava (OFU-04-05; Y = 32.0 ppm, La = 38.5, K = 11,539 ppm, Nd = 44.1, Ce = 81.9). A mixing line has been calculated for trace elements (gray hatched line). The contribution of a trachytic MI composition to the mixture that is required to generate the most evolved and highest $^{87}Sr/^{86}Sr$ lava from Samoa is about 70%–80%, consistent with that proposed by Adams et al. (2021).

a low $^{87}Sr/^{86}Sr$, mafic endmember and a high $^{87}Sr/^{86}Sr$, evolved composition representing the EM2-derived endmember (Adams et al., 2021; Edwards et al., 2019; Jackson et al., 2007). While EM2 has high $^{87}Sr/^{86}Sr$ and EM2 lavas at Samoa are relatively evolved, previous work has shown that EM2 cannot be derived from shallow contamination by assimilation of sediments (Jackson et al., 2007) or oceanic crustal material, given that oceanic crust has insufficient radiogenic $^{87}Sr/^{86}Sr$ to produce the values of the ALIA-D115 lavas. Furthermore, the Pb isotopic compositions of modern marine sediments in the Samoan region and the ALIA-D115 lavas form a diverging, non-overlapping trend such that the highest $^{87}Sr/^{86}Sr$ lavas are *furthest* from the marine sediment field (see the following work for more detail: Jackson et al., 2007; Edwards et al., 2019). Adams et al. (2021) present high precision Sr and Nd isotope measurements on individual clinopyroxene porphyrocrysts from the ALIA-D115-18 whole rock lava, and reveals the highest $^{87}Sr/^{86}Sr$ (0.723888) ever recorded for the oceanic mantle (for comparison, the highest $^{87}Sr/^{86}Sr$ for an ALIA-D115 whole rock is 0.720469; Jackson et al., 2007). Thus, the EM2-derived endmember melt must have $^{87}Sr/^{86}Sr$ at least as high

as this value. Adams et al. (2021) advances the knowledge of the EM2-derived mixing endmember by using the compositions of ALIA-D115 whole rock lavas, together with magma mixing theory, to derive estimates of the compositions of the two magma mixing endmembers contributing to the ALIA-D115 magmatic suite. The generation of the ALIA-D115 lava compositions requires a mafic, low $^{87}Sr/^{86}Sr$ endmember and an endmember with high $^{87}Sr/^{86}Sr$ and high SiO_2 (i.e., the EM2-derived endmember). Potential EM2-derived mixing endmembers calculated by Adams et al. (2021) are trachytic in composition (SiO_2 = 62.2–65.5 wt%, MgO = 0.5–2 wt%, $Na_2O + K_2O$ = 10–11 wt%) with estimated $^{87}Sr/^{86}Sr$ values between 0.7249 and 0.7316. Remarkably, the range of EM2-derived endmember melt compositions from Adams et al. (2021) overlap the reconstructed trachytic MIs presented in this study (Figure 4). Thus, the question remains: what is the origin of these trachytic MIs? Are they melts formed by fractional crystallization of a mafic parental melt that was characterized by radiogenic $^{87}Sr/^{86}Sr$? Or do they represent partial or total melts of a more silica-rich and higher $^{87}Sr/^{86}Sr$ source material? In the case of the latter, the reactivity of such relatively high-silica melts in an ultramafic (peridotitic) mantle is problematic for their mobility. In either case, the MIs were captured during the magma mixing process that formed the ALIA-D115 lavas.

Results of this study suggest the reconstructed MIs are remarkably similar to an independently derived EM2-mixing endmember proposed by Adams et al. (2021). In order to further assess this hypothesis, we can compare the MI chemistry with that of the ALIA-D115 whole rocks, other Samoan whole rock lavas, and Samoan pillow glasses to better understand the mixing process. Figure 4 shows major element variation of the ALIA-D115-18 MIs with whole rock lava compositions from the ALIA-D115 and other Samoan whole rock lavas and pillow glasses. The ALIA-D115 lavas form an array extending from the more primitive Samoan whole rocks toward the ALIA-D115-18 melt inclusions. Also shown are two EM2 mixing endmembers proposed by Adams et al. (2021), one a lower MgO trachytic endmember (green star), a higher MgO tracytic endmember (pink star), and a calculated mafic mixing endmember (black star). The major element composition of the EM2-derived mixing endmembers overlaps with the major element composition of the melt inclusions of this study, with the exception of FeO, which is about 1.5–3.0 wt% lower in the ALIA-D115 MIs than the inferred EM2-derived endmember. This suggests that the MIs could in fact be representative of the EM2-derived mixing endmember predicted by Adams et al. (2021). However, in major element space (Figure 4), the trend formed by ALIA-D115 whole rock lavas could be mistaken for a fractional crystallization trend (with the mineral assemblage olivine + clinopyroxene + plagioclase + ilmenite). Nevertheless, unequivocal evidence of the MIs being a mixing endmember of the ALIA-D115 lavas is seen in trace element and isotope space (Figures 5 and 6).

In comparison of the LREE and K with Y (Figure 5), the Samoan whole rock lavas and pillow glasses form a linear, positively sloping fractional crystallization trend, whereas the ALIA-D115 lavas form an orthogonal (and negatively sloping) trend connecting the array formed by Samoan lavas with the array formed by the Samoan MIs. As an example, Figure 5 presents a comparison of K and Y (where both elements are incompatible in the suite of phases observed in the host lava and melt inclusions), where the ALIA-D115 lavas show a negatively sloping trend, nearly orthogonal to that of the other Samoan lavas and pillow glasses, that cannot be the result of fractional crystallization. This is because fractional crystallization will generate positively-sloping trends for incompatible elements like K and Y (as can be seen for the other Samoan lavas and pillow glasses). Therefore, we argue that the trend formed by the ALIA-D115 lavas is the result of magma mixing in which the trachytic MIs represent one mixing endmember and the Samoan basalts reflect the other mixing endmember; this is consistent with the results of Adams et al. (2021), who identified the ALIA-D115 lavas to be the result of mixing between a mafic (low $^{87}Sr/^{86}Sr$) and a silicic (high $^{87}Sr/^{86}Sr$) endmember. Although we cannot yet measure the $^{87}Sr/^{86}Sr$ in the MIs due to their small size, their isotopic compositions can be inferred by extrapolating existing trends in the Samoan magmatic suite. Figure 6 shows $^{87}Sr/^{86}Sr$ versus SiO_2 and K_2O for the ALIA-D115 whole rocks, other Samoan whole rocks, and two mixing endmembers of Adams et al. (2021). The data support a mixing trend for the ALIA-D115 whole rock lavas, where lavas associated with higher SiO_2 and K_2O have higher $^{87}Sr/^{86}Sr$. Using this trend, we can extrapolate $^{87}Sr/^{86}Sr$ compositions by employing the SiO_2 and K_2O concentrations of the melt inclusions. An extrapolation of the ALIA-D115 mixing trend into the range of SiO_2 and K_2O observed in the MIs show that on average, the MIs could have a $^{87}Sr/^{86}Sr$ of ~0.725, which is within range of the values predicted by Adams et al. (2021; Figure 6). Lastly, further evidence that the MIs could represent a mixing endmember is that one melt inclusion hosts two Fo_{73} olvines, not in equilibrium with a trachytic liquid, and indicative of interaction

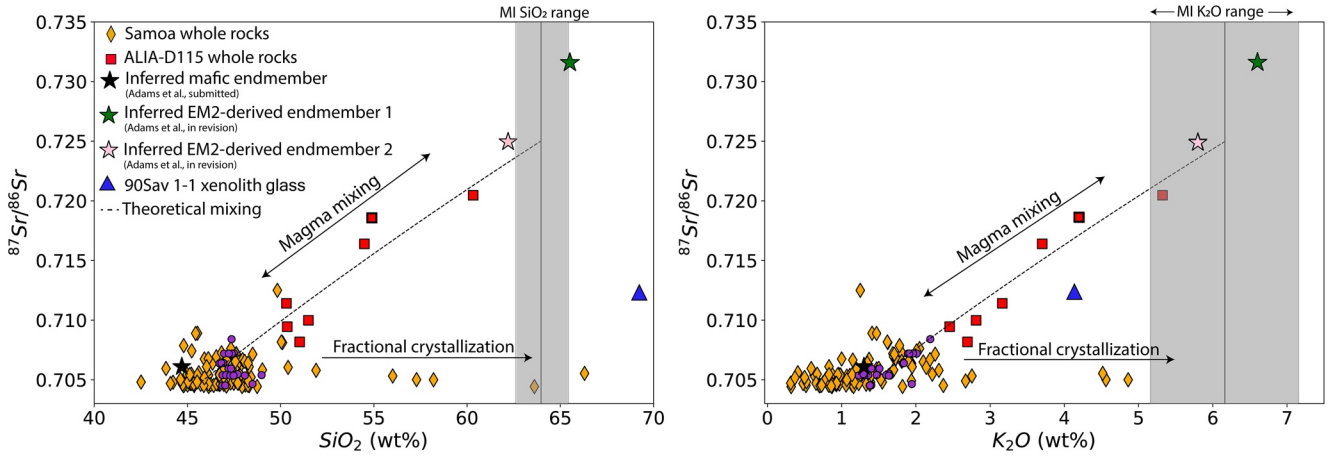

Figure 6. $^{87}Sr/^{86}Sr$ versus SiO_2 and K_2O comparing Samoan whole rock lavas (orange diamonds), ALIA-D115 whole rock lavas (red squares; data from Jackson et al., 2007; the ALIA-D115-18 sample is outlined in bold), Samoa pillow glass (purple circles), a high silica (trachytic), high $^{87}Sr/^{86}Sr$ Savai'i xenolith glass (Hauri et al., 1993; dark blue triangles), and the inferred mafic (black star) and two silicic mixing endmembers (low MgO EM2 silicic endmember 1 = green star, high MgO EM2 silicic endmember 2 = pink star) calculated by Adams et al. (2021). The figure allows an estimate of the $^{87}Sr/^{86}Sr$ composition of the melt inclusions (not yet measured) using whole rock trends and melt inclusion major element compositions. The gray shaded region is the range of SiO_2 and K_2O values in the reconstructed MIs of this study. The thick gray line within the gray shaded region is the average MI value. The dashed line is a mixing line through the ALIA-D115 lavas, which is shown to illustrate an extension of this mixing array into the MI composition space (gray shaded region). The mafic mixing endmember is the same Ofu lava used in the previous mixing figures and the silicic mixing endmember uses the average MI SiO_2, K_2O, and Sr concentration to estimate the $^{87}Sr/^{86}Sr$ value. The dashed mixing line (showing little curvature due to the similarity of Sr concentration between the two mixing endmembers) meets the average MI value at a $^{87}Sr/^{86}Sr$ value of ~0.725 for both the SiO_2 and K_2O plots. This value is within the range of values calculated by Adams et al. (2021), but is most similar to the value calculated for the higher MgO EM2 endmember of 0.7249. We chose to use an MI composition as an EM2 mixing endmember instead of those calculated by Adams et al. (2021) because we wanted to independently evaluate whether the MIs correspond to these previously calculated endmembers.

with a more mafic magma. Thus, there are multiple lines of evidence that interaction of mafic and silicic magmas played a central role in the formation of the ALIA-D115 lavas, and the melt inclusions provide us with the first glimpse of actual melts that match the trachytic composition of the EM2 endmember melt predicted by Adams et al. (2021).

After reconstruction for PEC, the Si-rich nature observed in the MIs represents the Si-rich nature of liquids captured during the formation of the ALIA-D115-18 whole rock and hosting clinopyroxenes. If the MIs are in fact melts that ultimately derived from an EM2 source, what process has controlled their composition? There are two obvious potential mechanisms that could explain the observed compositions: 1) the EM2-derived liquids began as mafic primary liquids that experienced significant fractional crystallization prior to entrapment and the MIs were captured by growing clinopyroxene, or 2) the MIs formed as a result of partial melting, to different degrees (highly affecting the trace element variability), of the EM2-derived source directly, with minor subsequent pre- or post-entrapment fractional crystallization (i.e., the primary mantle melts were silicic).

In reality, it is likely a combination of both mechanisms, but a few points seem clear: 1) the enrichment in LREEs compared with HREEs is indicative of garnet in the petrogenesis of the melt inclusions (Figure 2), and 2) if the melt inclusions were a result of originally mafic melts that underwent significant fractional crystallization, we expect that their trace element signatures would reflect this process. Trace element signatures in Figure 2 show that the MIs exhibit depletions in Nb and Ti, which could be related to removal of Ti-rich phases, like ilmenite (i.e., during crystallization after partial melting from the source). The Nb and Ti depletion could also be due to ilmenite crystallization after entrapment, however, PEC of ilmenite appears to be minimal in these inclusions with the exception of one MI (mt1gr11) in which the ilmenite appears to have intergrown with olivine and been trapped along with the MI. Additionally, the host clinopyroxenes themselves are depleted in Nb and Ti, suggesting ilmenite removal prior to their growth. The MIs are depleted in Sc (Data Set S2) relative to the ALIA-D115 lavas (Jackson et al., 2007), suggesting that they could have had significant clinopyroxene removal as well, during pre- and post-entrapment. This seems reasonable as ilmenite and clinopyroxene are common phases present in the ALIA-D115 lavas. However, another very

common phase in the ALIA-D115 lavas is plagioclase, which is never seen in any of the MIs of this study. If the MIs had undergone significant differentiation prior to entrapment, plagioclase would likely have been removed, but this is certainly not the case as the MIs are quite enriched in Sr: while some inclusions exhibit slight negative Sr anomalies—the hallmark of plagioclase crystallization—many do not (some show positive anomalies, some show no anomaly, and others show negative anomalies; Figure 2). Further, we note this is likely not a result of pressure or water effects suppressing plagioclase crystallization according to fractional crystallization simulations using MELTS (performed for the PEC calculations as described in the Methods section) and the reconstructed MI compositions as the starting bulk compositions. MELTS simulations were performed at a range of pressures and water concentrations (where water concentrations were those of the reconstructed MI bulk compositions and show plagioclase saturation shortly after clinopyroxene crystallization begins in all simulations. More specifically, plagioclase saturates ~5 ^{o}C–50 ^{o}C after initiation of clinopyroxene crystallization, corresponding to ~2–15% fractionation of the original liquid bulk composition, with the variability in saturation temperature depending predominately on the water concentration of the MI (i.e., as MI water concentrations increase, the change in temperature between clinopyroxene and plagioclase saturation increases, with plagioclase saturating at increasingly lower temperatures after clinopyroxene saturation at the liquidus). This suggests that plagioclase removal is not responsible for the high silica nature of the inclusions. Thus, it seems that the argument that the MIs owe their ultimate origin to mantle-derived mafic melts that underwent *significant* differentiation is ambiguous, and does not fit the MI geochemistry. Alternatively, if the trachytic liquids in the MIs are a direct result of partial melting of a mantle source (i.e., the primary mantle-derived melts were trachytic), how have these liquids survived without reacting with the surrounding peridotite mantle during ascent through the asthenosphere and oceanic mantle lithosphere?

There are a few possibilities that could explain the origin of the trachytic MIs. One of the simplest explanations is that they are derived from partial melting of a sediment or sediment-enriched source. These melts then mix with more primitive Samoan basaltic melt (derived by partial melting of peridotite) to create the ALIA-D115 mixing trend. Problematically, this requires silicic melts to remain isolated from the ambient ultramafic mantle—including during ascent through >60 km of Pacific mantle lithosphere—until time of mixing with the basaltic magmas in shallow magma chambers. It has been previously documented that siliceous melts are highly reactive with ultramafic bulk compositions (Arai et al., 2003; Bianchini et al., 2011, 2015; Shimizu et al., 2004). Nevertheless, there is evidence for isolation of silica-rich veins in peridotite mantle xenoliths found in alkali basalts from Tallante, Spain. The high-silica narrow dikes (quartz-diorite bulk composition) are thought to be the result of slab melts that are able to remain isolated form the surrounding mantle through an initial reaction between the high silica activity silicate melt and low silica activity olivine creating an orthopyroxene reaction barrier at the contact, via the classic reaction relationship of $SiO_2 + Mg_2SiO_3 = 2MgSiO_3$ (i.e., a reaction between the silicic melts and the peridotite wallrock;Arai et al., 2003; Bianchini et al., 2011, 2015; Shimizu et al., 2004). However, the Tallante xenoliths record a process that occurred at the cm-scale. In order for the process to transport trachytic liquids out of the mantle source, it would have to operate on a larger scale, allowing the trachyte liquid + peridotite reaction to create opx-rich wall rock to buffer the silicate melts, allowing transport >60 km through the peridotite oceanic mantle lithosphere without completely reacting with the surrounding peridotite. However, if this process does occur at Samoa, where conduits transporting trachytic melts are mantled by opx to facilitate melt transport to the surface, then a key question is why do we not see these silicic primary liquids erupted at other hotspot locations, like Hawaii, where partial melting of Si-saturated eclogite yields Si-rich liquids (Hauri, 1996; Sobolev, 2007; Sobolev et al, 2000, 2005; Yaxley & Sobolev, 2007).

Another explanation for the formation of the trachytic MIs is a scenario in which ancient recycled sediment, captured by the Samoan plume source, partially melts and fertilizes the surrounding mantle to form a hybridized peridotite + sediment mixture. Thermodynamic phase equilibria modeling by Adams et al. (2021) of various hybrid peridotite + sediment bulk compositions suggests that the partial melts are basanitic to phonolititc (depending on the extent of melting) and that subsequent differentiation of these melts does not lead to trachytic liquids. That being said, the exploratory model space is quite large and these models capture a small portion of conceivable starting compositions (including the fraction of recycled sediment, fraction of peridotite, and/or fraction of recycled mafic material), pressures, percentage of source melting prior to differentiation, redox conditions, total volatiles, etc. There are some experimental studies, however,

that show partial melting of hybridized peridotite + sediment-like bulk compositions can in fact produce trachytic liquids similar to the MIs of this study (Gao et al., 2019; Wang et al., 2017). However, the same problem noted earlier remains: how are silicic liquids transported through the peridotitic mantle lithosphere to the surface without reacting with the wall rock?

Lastly, there is evidence that the EM2 source has been enriched not only by addition of sediments, but also carbonatitic material. Carbonatitic metasomatism beneath Samoa has been proposed by many authors (Ashley, 2019; Ashley et al., 2020; Hauri et al., 1993; Hauri & Hart, 1994). Evidence for carbonatite metasomatism is clearest in Samoan mantle peridotite xenoliths that show evidence of interaction with carbonatitic liquids based on their LREE enrichment and Zr and Ti depletions in clinopyroxene (Hauri & Hart, 1994; Hauri et al., 1993). More recently, Ashley et al. (2020) performed an analysis of water systematics and major and trace element characteristics in Samoa peridotite xenoliths (focusing on orthopyroxenes) revealing variable depletions in water contents of nominally anhydrous minerals, and in addition to their trace element characteristics, indicate metasomatism of carbonatitic and silicate liquids. Further, previous studies have suggested that partial melting of mantle enriched with carbonatitic liquids can result in phonolitic to trachytic liquids (Ashwal et al., 2016; Hauri et al., 1993; Loges et al., 2019; Tsuno and Dasgupta, 2011). To this end, Hauri et al. (1993) found trachytic glass (69% SiO_2, 8% total alkalis; see main text Figures 3–6 for plotted compositions of the glass) hosted in a carbonatite metasomatized peridotite xenolith from the Samoan island of Savai'i—the same volcano that erupted the ALIA-D115-18 melt inclusions examined here—which they interpret to be the product of a reaction between carbonatitic melt with peridotite. Critically, this liquid is nearly trachytic and has elevated $^{87}Sr/^{86}Sr$ (0.712344)—further suggesting a *potential* role for carbonatitic metasomatism in the origin of EM2 and supporting the presence of high silica melts in the mantle. An important question to address is whether sufficient trachytic melt with high $^{87}Sr/^{86}Sr$ values can be generated in metasomatic peridotites, and sequestered into crustal magma chambers, to give rise to the Si-rich Samoan EM2 endmember lavas and the trachytic melt inclusions they host.

5. Conclusions

Three key questions were raised in this work: 1) Have the trachytic MIs been significantly modified by post-entrapment processes, 2) how are the trachytic MIs related to their host whole rock and the other ALIA-D115 lavas, and 3) what is the origin of the trachytic MIs? We believe the MIs, after compositional reconstruction that involves clinopyroxene addition, represent the most extreme EM2 compositions in global OIB. In both major and trace element space, the MIs lay at one end of the ALIA-D115 mixing array, suggesting the silicic MIs are the high $^{87}Sr/^{86}Sr$ mixing endmember with an affinity to EM2. This idea is consistent with previous studies that the melts derived from the EM2 mixing endmember beneath Samoa are highly evolved and geochemically enriched (high in $^{87}Sr/^{86}Sr$). Projecting the ALIA-D115 mixing trend in $^{87}Sr/^{86}Sr$ versus SiO_2 space and in $^{87}Sr/^{86}Sr$ versus K_2O space shows that the trend intersects the average MI composition at $^{87}Sr/^{86}Sr$ values of ~0.725 (consistent for both SiO_2 and K_2O), which is within the range of the independently calculated values predicted by Adams et al. (2021) of 0.7249–0.7316. Trace element signatures suggest the MIs could have undergone some fractionation prior to entrapment in the clinopyroxenes. Alternatively, the MIs could be representative of melts derived directly from the EM2 source with little fractionation prior to entrapment, but this requires that the trachytic liquids were somehow preserved against reaction with peridotitic mantle during vertical transport through 60 km of oceanic mantle lithosphere. Further partial melting thermodynamic calculations of potential EM2 source compositions as well as laboratory studies of partial melting of various mafic and ultramafic sources subject to sediment addition or modification by metasomatism should be further explored to better understand the formation of these trachytic melt inclusions.

Data Availability Statement

All geochemical data from this study are available in the Supporting data sets of this article and can also be found on the IEDA EarthChem online database at the following link: https://doi.org/10.26022/IEDA/111729.

Acknowledgments
M. G. Jackson acknowledges the mentorship and generosity of Erik H. Hauri, who provided unfettered access to microbeam facilities during his 16-months tenure as a post-doc at DTM. M. G. Jackson also acknowledges support from NSF grants OCE-1912931, EAR-1900652, and OCE-1736984. The authors thank Stan Hart and Hubert Staudigel for generously providing us with a Samoan sample for this work. J. V. Adams acknowledges Gareth Seward and John Cottle for help with major and trace element analyses on the clinopyroxenes. All authors would like to thank Michael Rowe, Leonid Danyushevsky, and one anonymous reviewer for their extremely constructive and helpful reviews that greatly improved this manuscript. The authors declare no conflicts of interest.

References

Adams, J. V., Jackson, M. G., Spera, F. J., Price, A. A., Byerly, B. L., Seward, G., & Cottle, J. M. (2021). Extreme isotopic heterogeneity in Samoan clinopyroxenes constrains sediment recycling. *Nature Communications*. *12*(1234). https://doi.org/10.1038/s41467-021-21416-9

Anderson, A. T., & Wright, T. L. (1972). Phenocrysts and glass inclusions and their bearing on oxidation and mixing of basaltic magmas, Kilauea Volcano, Hawaii. *American Mineralogist*, *57*, 188–216.

Arai, B. S., Shimizu, Y., & Gervilla, F. (2003). Quartz diorite veins in a peridotite xenolith from Tallante, Spain: Implications for reaction and survival of slab-derived SiO_2-oversaturated melt in the upper mantle. *Proceedings of the Japan Academy, Series B*, *79*(6), 145–150.

Ashley, A. W. (2019). Water systematics of Samoan peridotite xenoliths (Master's thesis). University of South Carolina. Retrieved from https://scholarcommons.sc.edu/etd/5315

Ashley, A. W., Bizimis, M., Peslier, A. H., & Jackson, M. (2020). Metasomatism and hydration of the oceanic lithosphere: A case study of peridotite xenoliths from Samoa. *Journal of Petrology*, *61*(2), egaa028. https://doi.org/10.1093/petrology/egaa028

Ashwal, L., Torsvik, T., Horváth, P., Harris, C., Webb, S., Werner, S., & Corfu, F. (2016). A mantle-derived origin for mauritian trachytes. *Journal of Petrology*, *57*(9), 1645–1676. https://doi.org/10.1093/petrology/egw052

Baker, D. R. (2008). The fidelity of melt inclusions as records of melt composition. *Contributions to Mineralogy and Petrology*, *156*(3), 377–395. https://doi.org/10.1007/s00410-008-0291-3

Bianchini, G., Beccaluva, L., Nowell, G. M., Pearson, D. G., & Siena, F. (2011). Mantle xenoliths from Tallante (Betic Cordillera): Insights into the multi-stage evolution of the south Iberian lithosphere. *Lithos*, *124*(3–4), 308–318. https://doi.org/10.1016/j.lithos.2010.12.004

Bianchini, G., Braga, R., Langone, A., Natali, C., & Tiepolo, M. (2015). Metasedimentary and igneous xenoliths from Tallante (Betic Cordillera, Spain): Inferences on crust-mantle interactions and clues for post-collisional volcanism magma sources. *Lithos*, *220–223*, 191–199. https://doi.org/10.1016/j.lithos.2015.02.011

Bucholz, C. E., Gaetani, G. A., Behn, M. D., & Shimizu, N. (2013). Post-entrapment modification of volatiles and oxygen fugacity in olivine-hosted melt inclusions. *Earth and Planetary Science Letters*, *374*, 145–155. https://doi.org/10.1016/j.epsl.2013.05.033

Cabral, R. A., Jackson, M. G., Koga, K. T., Rose-Koga, E. F., Hauri, E. H., Whitehouse, M. J., et al. (2014). Volatile cycling of H_2O, CO_2, F, and Cl in the HIMU mantle: A new window provided by melt inclusions from oceanic hot spot lavas at Mangaia, Cook Islands. *Geochemistry, Geophysics, Geosystems*, *15*(11), 4445–4467. https://doi.org/10.1002/2014gc005473

Cottrell, E., Spiegelman, M., & Langmuir, C. H. (2002). Consequences of diffusive reequilibration for the interpretation of melt inclusions. *Geochemistry, Geophysics, Geosystems*, *3*(5), 1–26. https://doi.org/10.1029/2001GC000205

Danyushevsky, L. V., Della-Pasqua, F. N., & Sokolov, S. (2000). Re-equilibration of melt inclusions trapped by magnesian olivine phenocrysts from subduction-related magmas: Petrological implications. *Contributions to Mineralogy and Petrology*, *138*(1), 68–83. https://doi.org/10.1007/PL00007664

Danyushevsky, L. V., Leslie, R. A. J., Crawford, A. J., & Durance, P. (2004). Melt inclusions in primitive olivine phenocrysts: The role of localized reaction processes in the origin of anomalous compositions. *Journal of Petrology*, *45*(12), 2531–2553. https://doi.org/10.1093/petrology/egh080

Danyushevsky, L. V., McNeill, A. W., & Sobolev, A. V. (2002). Experimental and petrological studies of melt inclusions in phenocrysts from mantle-derived magmas: An overview of techniques, advantages and complications. *Chemical Geology*, *183*(1–4), 5–24. https://doi.org/10.1016/S0009-2541(01)00369-2

Edwards, M. A., Jackson, M. G., Kylander-Clark, A. R. C., Harvey, J., Hagen-Peter, G. A., Seward, G. G. E., et al. (2019). Extreme enriched and heterogeneous 87Sr/86Sr ratios recorded in magmatic plagioclase from the Samoan hotspot. *Earth and Planetary Science Letters*, *511*, 190–201. https://doi.org/10.1016/j.epsl.2019.01.040.

Gaetani, G. A., & Watson, E. B. (2000). Open system behavior of olivine-hosted melt inclusions. *Earth and Planetary Science Letters*, *183*(1–2), 27–41. https://doi.org/10.1016/S0012-821X(00)00260-0

Gaetani, G. A., & Watson, E. B. (2002). Modeling the major-element evolution of olivine-hosted melt inclusions. *Chemical Geology*, *183*(1–4), 25–41. https://doi.org/10.1016/S0009-2541(01)00370-9

Gaetani, G. A., O'Leary, J. A., Shimizu, N., Bucholz, C. E., & Newville, M. (2012). Rapid reequilibration of H2O and oxygen fugacity in olivine-hosted melt inclusions. *Geology*, *40*(10), 915–918. https://doi.org/10.1130/G32992.1

Gao, M., Xu, H., Zhang, J., & Foley, S. F. (2019). Experimental interaction of granitic melt and peridotite at 1.5 GPa: Implications for the origin of post-collisional K-rich magmatism in continental subduction zones. *Lithos*, *350–351*(October), 105241. https://doi.org/10.1016/j.lithos.2019.105241

Ghiorso, M. S., & Sack, R. O. (1995). Chemical mass transfer in magmatic processes IV. A revised and internally consistent thermodynamic model for the interpolation and extrapolation of liquid-solid equilibria in magmatic systems at elevated temperatures and pressures. *Contributions to Mineraology and Petrology*, *119*, 197–212.

Gualda, G. A. R., Ghiorso, M. S., Lemons, R. V., & Carley, T. L. (2012). Rhyolite-MELTS: A modified calibration of MELTS optimized for silica-rich, fluid bearing magmatic systems. *Journal of Petrology*, *52*, 875–890.

Hart, S., & Jackson, M.G. (2014). Ta'u and Ofu/Olosega volcanoes: The "twin sisters" of Samoa, their P, T, X melting regime, and global implications. *Geochemistry, Geophysics, Geosystems*, *15*(6), 2301–2318. https://doi.org/10.1002/2013GC005221

Hauri, E. (2002). SIMS analysis of volatiles in silicate glasses, 2: Isotopes and abundances in Hawaiian melt inclusions. *Chemical Geology*, *183*(1–4), 115–141. https://doi.org/10.1016/S0009-2541(01)00374-6

Hauri, E. H. (1996). Major-element variability in the Hawaiian mantle plume. *Nature*, *382*(6590), 415–419.

Hauri, E. H., & Hart, S. R. (1994). Constraints on melt migration from mantle plumes: A trace element study of peridotite xenoliths from Savai'i, Western Samoa. *Journal of Geophysical Research*, *99*(B12), 24301–24321. https://doi.org/10.1029/94jb01553

Hauri, E. H., Shimizu, N., Dieu, J. J., & Hart, S. R. (1993). Evidence for hotspot-related carbonatite metasomatism in the oceanic upper mantle. *Nature*, *365*(6443), 221–227. https://doi.org/10.1038/365221a0

Jackson, M. G., & Hart, S. R. (2006). Strontium isotopes in melt inclusions from Samoan basalts: Implications for heterogeneity in the Samoan plume. *Earth and Planetary Science Letters*, *245*(1–2), 260–277. https://doi.org/10.1016/j.epsl.2006.02.040

Jackson, M. G., Hart, S. R., Koppers, A. A., Staudigel, H., Konter, J., Blusztajn, J., et al. (2007). The return of subducted continental crust in Samoan lavas. *Nature*, *448*(9), 684–687. https://doi.org/10.1038/nature06048

Jackson, M. G., & Shirey, S. B. (2011). Re-Os isotope systematics in Samoan shield lavas and the use of Os-isotopes in olivine phenocrysts to determine primary magmatic compositions. *Earth and Planetary Science Letters*, *312*(1–2), 91–101. https://doi.org/10.1016/j.epsl.2011.09.046

Kamenetsky, V. (1996). Methodology for the study of melt inclusions in Cr-spinel, and implications for parental melts of MORB from FAMOUS area. *Earth and Planetary Science Letters*, *142*(3–4), 479–486. https://doi.org/10.1016/0012-821x(96)00117-3

Kamenetsky, V. S., Crawford, A. J., Eggins, S., & Mühe, R. (1997). Phenocryst and melt inclusion chemistry of near-axis seamounts, Valu Fa Ridge, Lau Basin: Insight into mantle wedge melting and the addition of subduction components. *Earth and Planetary Science Letters*, *151*(3–4), 205–223. https://doi.org/10.1016/s0012-821x(97)81849-3

Kent, A. J. R. (2008). Melt inclusions in basaltic and related volcanic rocks. *Reviews in Mineralogy and Geochemistry*, *69*, 273–332.

Kent, A. J. R., & Elliott, T. R. (2002). Melt inclusions from Marianas arc lavas: Implications for the composition and formation of island arc margins. *Chemical Geology*, *183*(1–4), 263–286. https://doi.org/10.1016/S0009-2541(01)00378-3

Kent, A. J. R., Norman, M. D., Hutcheon, I. D., & Stolper, E. M. (1999). Assimilation of seawater-derived components in an oceanic volcano: Evidence from matrix glasses and glass inclusions from Loihi seamount, Hawaii. *Chemical Geology*, *156*(1–4), 299–319. https://doi.org/10.1016/S0009-2541(98)00188-0

Kress, V. C., & Ghiorso, M. S. (2004). Thermodynamic modeling of post-entrapment crystallization in igneous phases. *Journal of Volcanology and Geothermal Research*, *137*(4), 247–260. https://doi.org/10.1016/j.jvolgeores.2004.05.012

Loges, A., Schultze, D., Klügel, A., & Lucassen, F. (2019). Phonolitic melt production by carbonatite Mantle metasomatism: evidence from Eger Graben xenoliths. *Contributions to Mineralogy and Petrology*, *174*(93), https://doi.org/10.1007/s00410-019-1630-2

Lowenstern, J. B. (1995). Applications of silicate-melt inclusions to the study of magmatic volatiles. Magmas, fluids and ore deposits. *Mineralogical Association of Canada Short Course*, *23*, 71–99.

Maclennan, J. (2008). Lead isotope variability in olivine-hosted melt inclusions from Iceland. *Geochimica et Cosmochimica Acta*, *72*(16), 4159–4176. https://doi.org/10.1016/j.gca.2008.05.034

Melson, W. G. (1983). Monitoring the 1980-1982 eruptions of Mount St. Helens: Composition and abundance of glass. *Science*, *221*(4618), 1387–1391.

Michael, P. J., McDonough, W. F., Nielsen, R. L., & Cornell, W. C. (2002). Depleted melt inclusions in MORB plagioclase: Messages from the mantle or mirages from the magma chamber? *Chemical Geology*, *183*(1–4), 43–61. https://doi.org/10.1016/S0009-2541(01)00371-0

Nielsen, R. L., Michael, P. J., & Sours-Page, R. (1998). Chemical and physical indicators of compromised melt inclusions. *Geochimica et Cosmochimica Acta*, *62*(5), 831–839. https://doi.org/10.1016/S0016-7037(98)00024-6

Peterson, M. E., Saal, A. E., Kurz, M. D., Hauri, E. H., Blusztajn, J. S., Harpp, K. S., et al. (2017). Submarine basaltic glass from the Galapgos Archipelago: Determining the volatile budget of the manlte plume. *Journal of Petrology*, *58*(7), 1419–1450. https://doi.org/10.1093/petrology/egx059

Plank, T., Kelley, K. A., Zimmer, M. M., Hauri, E. H., & Wallace, P. J. (2013). Why do Mafic arc magmas contain ~4 wt % water on average? How much water comes out arc volcanoes? *Earth and Planetary Science Letters*, *364*, 168–179.

Portnyagin, M., Almeev, R., Matveev, S., & Holtz, F. (2008). Experimental evidence for rapid water exchange between melt inclusions in olivine and host magma. *Earth and Planetary Science Letters*, *272*(3–4), 541–552. https://doi.org/10.1016/j.epsl.2008.05.020

Qin, Z., Lu, F., & Anderson, A. T. (1992). Diffusive reequilibration of melt and fluid inclusions. *American Mineralogist*, *77*(5–6), 565–576.

Reinhard, A. A., Jackson, M. G., Koornneef, J. M., Rose-Koga, E. F., Blusztajn, J., Konter, J. G., et al. (2018). Sr and Nd isotopic compositions of individual olivine-hosted melt inclusions from Hawai'i and Samoa: Implications for the origin of isotopic heterogeneity in melt inclusions from OIB lavas. *Chemical Geology*, *495*, 36–49. https://doi.org/10.1016/j.chemgeo.2018.07.034

Roedder, E. (1984). Fluid inclusions. *Reviews in Mineralogy*, *12*, 1–644.

Rowe, M. C., Peate, D. W., & Newbrough, A. (2011). Compositional and thermal evolution of olivine-hosted melt inclusions in small-volume basaltic eruptions: A "simple" example from Dotsero Volcano, NW Colorado. *Contributions to Mineralogy and Petrology*, *161*(2), 197–211. https://doi.org/10.1007/s00410-010-0526-y

Saal, A. E., Hart, S. R., Shimizu, N., Hauri, E. H., & Layne, G. D. (1998). Pb isotopic variability in melt inclusions from oceanic Island Basalts, Polynesia. *Science*, *282*(5393), 1481–1484. https://doi.org/10.1126/science.282.5393.1481

Schiano, P., & Bourdon, B. (1999). On the preservation of mantle information in ultramafic nodules: Glass inclusions within minerals versus interstitial glasses. *Earth and Planetary Science Letters*, *169*(1–2), 173–188. https://doi.org/10.1016/S0012-821X(99)00074-6

Shimizu, Y., Arai, S., Morishita, T., Yurimoto, H., & Gervilla, F. (2004). Petrochemical characteristics of felsic veins in mantle xenoliths from Tallante (SE Spain): An insight into activity of silicic melt within the mantle wedge. *Special Papers – Geological Society of America*, *389*, 265–276. https://doi.org/10.1130/0-8137-2389-2.265

Sinton, C. W., Christie, D. M., Coombs, V. L., Nielsen, R. L., & Fisk, M. R. (1993). Near-primary melt inclusions in anorthite phenocrysts from the Galapagos Platfrom. *Earth and Planetary Science Letters*, *119*(4), 527–537. https://doi.org/10.1016/0012-821x(93)90060-M

Sobolev, A. V. (1996). Melt inclusions in minerals as a source of principle petrological information. *Petrology*, *4*(3), 209–220.

Sobolev, A. V. (2007). Melt inclusions and host olivines: What do they tell about mantle processes and sources. *Geochimica et Cosmochimica Acta*, *71*(15), A951.

Sobolev, A. V., Hofmann, A. W., & Nikogosian, I. K. (2000). Recycled oceanic crust observed in "ghost plagioclase" within the source of Mauna Loa lavas. *Nature*, *404*, 986–990. https://doi.org/10.1038/35010098

Sobolev, A. V., Hofmann, A. W., Sobolev, S. V., & Nikogosian, I. K. (2005). An olivine-free mantle source of Hawaiian shield basalts. *Nature*, *434*(7033), 590–597. https://doi.org/10.1038/nature03411

Sobolev, A. V., & Shimizu, N. (1993). The origin of typical NMORB: The evidence from a melt inclusions study. *Mineralogical Magazine*, *58A*(2), 862–863. https://doi.org/10.1180/minmag.1994.58a.2.184

Sours-Page, R., Johnson, K. T. M., Nielsen, R. L., & Karsten, J. L. (1999). Local and regional variation of MORB parent magmas: Evidence from melt inclusions from the endeavour segment of the Juan de Fuca Ridge. *Contributions to Mineralogy and Petrology*, *134*(4), 342–363. https://doi.org/10.1007/s004100050489

Spandler, C., O'Neill, H. S. C., & Kamenetsky, V. S. (2007). Survival times of anomalous melt inclusions from element diffusion in olivine and chromite. *Nature*, *447*(7142), 303–306. https://doi.org/10.1038/nature05759

Wallace, P. J. (2005). Volatiles in subduction zone magmas: Concentrations and fluxes based on melt inclusion and volcanic gas data. *Journal of Volcanology and Geothermal Research*, *140*(1–3), 217–240. https://doi.org/10.1016/j.jvolgeores.2004.07.023

Wang, Y., Prelević, D., Buhre, S., & Foley, S. F. (2017). Constraints on the sources of post-collisional K-rich magmatism: The roles of continental clastic sediments and terrigenous blueschists. *Chemical Geology*, *455*, 192–207. https://doi.org/10.1016/j.chemgeo.2016.10.006

White, W. M., & Hofmann, A. W. (1982). Sr and Nd isotope geochemistry of oceanic basalts and mantle evolution. *Nature*, *296*(5860), 821–825. https://doi.org/10.1038/296821a0

Yaxley, G. M., & Sobolev, A. V. (2007). High-pressure partial melting of gabbro and its role in the Hawaiian magma source. *Contributions to Mineralogy and Petrology*, *154*(4), 371–383. https://doi.org/10.1007/s00410-007-0198-4

References From the Supporting Information

Cherniak, D. J., & Dimanov, A. (2010). Diffusion in pyroxene, mica and amphibole. *Reviews in Mineralogy and Geochemistry*, *72*(1), 641–690. https://doi.org/10.2138/rmg.2010.72.14

Jochum, K. P., Weis, U., Stoll, B., Kuzmin, D., Yang, Q., Raczek, I., et al. (2011). Determination of reference values for NIST SRM 610-617 glasses following ISO guidelines. *Geostandards and Geoanalytical Research*, *35*, 397–429.

Geochemistry, Geophysics, Geosystems

Supporting Information for

Trachytic Melt Inclusions Hosted in Clinopyroxene Offer a Glimpse into Samoan EM2-endmember Melts

J. V. Adams[1*†], F. J. Spera[1], and M. G. Jackson[1]

[1]Department of Earth Science, University of California Santa Barbara, Santa Barbara, CA 93106, USA ([*]Corresponding author)

Contents of this file

Additional Supporting Information (Files uploaded separately)

Six supporting datasets

Introduction

Supporting dataset S1 consists of the trace element analysis of the secondary standard ALV 519-4-1 performed during melt inclusion trace element analysis. Supporting dataset S2 consists of major and trace element analyses of melt inclusions, their clinopyroxene hosts, as well as compositions of select daughter crystal inclusions. The major and trace element melt inclusion data and clinopyroxene major element data was collected at the Carnegie Institute of Washington. The clinopyroxene trace element data was collected at the University of California Santa Barbara (see Methods section of the main text for more details). Supporting dataset S3 contains the analyzed NIST612 reference material composition used during the LA-ICP-MS clinopyroxene trace element analysis. The supporting text, figures, and datasets S4 and S5 presented below are an analysis of geochemical gradients within clinopyroxenes hosting melt inclusions. Major and trace element analyses were performed on four clinopyroxene grains in the form of chemical transects extending from near a melt inclusion edge into the host clinopyroxene grain. The major and trace element data was collected at the University of California Santa Barbara EPMA and LA-ICP-MS laboratories (see Methods section in the main text for more details). The supporting text describes the chemical transects in detail and whether or not they are indicative of post-entrapment crystallization of the host clinopyroxene

from the melt inclusions. Supporting dataset S6 contains reconstructed melt inclusion compositions from post-entrapment crystallization corrections.

Text S1.

S1.1 Compositional gradients as a result of post-entrapment crystallization

Here we test post-entrapment crystallization of clinopyroxene as the mechanism generating the unusual melt inclusion compositions observed here. If we assume that the melt inclusions (MIs) represent a residual liquid from which host clinopyroxene grew after entrapment, we can consider a hypothetical model, as seen in Figure S1, that can be tested. In this model, the initial state of the MI is entrapment within the host clinopyroxene grain as shown in Figure S1a. After cooling proceeds, the MI begins to react with the host clinopyroxene and crystallize a compositionally distinct clinopyroxene at the MI edge (Figure S1b). If we assume no diffusive re-equilibration has occurred (the diffusion assumption is tested in Figures S2-S9), then we should observe major and trace element compositional gradients going away from the MI and into the host clinopyroxene (see Figure S1b A-A'). If crystallization is in equilibrium, we would expect compositional profiles to differ based on their partition coefficients (K_d) between clinopyroxene and melt. At location 1 along the A-A' transect in Figure S1c, we would expect compatible elements to have elevated concentrations (as this was the first clinopyroxene to grow from the melt), and low concentrations at location 2 (as this was the last clinopyroxene to grow from the melt). The incompatible elements will show the opposite behavior. We have measured 17 compositional profiles in 4 clinopyroxenes hosting melt inclusions and we can use this data to test if our incompatible and compatible element profiles are consistent with the model behavior.

S1.2 Major element profiles

Figures S2-S9 show 2-6 compositional profiles across each of the 4 clinopyroxene grains tested. Although we assume no diffusive re-equilibration has occurred, it behooves us to focus on the elements that diffuse the slowest as these are least affected by diffusion and preserve gradients (if any) resulting from the proposed PEC model (as shown in Figure S1). Compatible major elements within clinopyroxene that diffuse slowly are Si, Ca, and Cr. Slowly diffusing incompatible elements are Al and Ti. Figures S2-S5 show major element compositional profiles (termed line segments, or LS) going in different directions away from the MI edge and into the host clinopyroxene. Our model above predicts that Si, Ca, and Cr concentrations should increase going away from the MI, while Al and Ti concentrations should decrease. The gradients are determined to be inconsistent with the model if they show opposite trends for what the model predicts (i.e., if Cr gradients in clinopyroxene decrease with distance from the MI but our model predicts the Cr gradient should increase) *or* if they are flat (i.e., no gradient within relevant uncertainty). Thus, of the 17 line segments across four clinopyroxenes, 4 (~24%) Si profiles are consistent with the PEC model and 13 (76%) are not consistent (11 of which are flat), 5 (~29%) Ca profiles are consistent with the model and 12 (~71%) are not (9 of which are flat), and finally 1 (~6%) Cr profile is consistent with the model and 16 (~94%) are not (12 of which are flat). As for the incompatible major elements, 4 (~24%) Ti profiles are consistent with the model, while 13 (~76%) are not (8 of which are flat), and 7 (~41%) Al profiles are consistent with the model, while 10 (~59%) are not (7 of which are flat).

S1.3 Trace element profiles

Thirteen of the 17 profiles analyzed for major elements by electron microprobe were later analyzed for trace elements by LA-ICP-MS (see the main text for Methods description). Figures S6-S9 show trace element compositional profiles for the same clinopyroxene as described for the major elements, but not all line segments were measured given the laser spot size and available space on the clinopyroxene. We can test our model again for incompatible (i.e., Y, Zr, La, Ce, Dy) and compatible elements (i.e., Sc). For the profiles presented in Figures S6-S9, the compatible element, Sc, should increase going away from the MI and 2 (~15%) out of the 13 transects are consistent with this hypothesis while 11 (~85%) are not (with 8 being flat within uncertainty). For the following incompatible elements: Zr, Y, La, Ce, Dy, and Nd, about 31-38% of the 13 profiles show agreement with the model (decreasing gradients going away from the MI) and 62-69% do not conform to the model. For Gd, Sm, and Ho, ~8-15% of the profiles are consistent with the model while 85-92% of the profiles are not consistent. For Yb, none of the profiles are consistent with the PEC model. It should be noted that many of the non-model conforming line profiles were either going in the opposite direction of the predicted model gradient or were ambiguous due to oscillatory zoning or were flat within uncertainty.

S1.4 Conclusions

Considering the combined major and trace element transect data, only 2 out of the 13 (~15%) profiles measured for both major and trace elements completely conform (meaning all elements both trace and major elements, incompatible and compatible, behave as the model predicts for PEC) to the PEC model presented here (these two profiles are found within separate clinopyroxene grains: Mt2gr11 LS1 and mt2gr12 LS4).

There is much ambiguity in interpreting some of these chemical gradients because some profiles within a single clinopyroxene can exhibit opposite behavior, as in some profiles will increase in concentration of compatible elements going away from the MI and some will decrease (e.g., see the four Cr_2O_3 profiles in Figure S5 in which profiles LS2 and LS4 increase going away from the MI and LS1 and LS3 decrease). The same feature is seen with the incompatible elements as well (see example in Figure S7 in which LS1 and LS3 of the Y and Zr profiles are decreasing going away from the MI while LS2 is increasing). This behavior could be due to clinopyroxene anisotropy, which has been previously observed (e.g., Biedermann et al., 2015). Regardless, there are a small number of profiles completely consistent with the PEC model presented here, and thus PEC has clearly played some role in modifying the MIs, but as discussed in the main text, is likely not significant enough to be the primary control for major and particularly trace element variability. To summarize, of the 4 clinopyroxene grains analyzed (which host a total of 5 melt inclusions reported in Supporting Dataset S2), only two clinopyroxenes exhibit a single compositional profile each that is completely consistent with PEC for both major and trace elements—other profiles in the same two grains are not consistent with PEC, making the PEC interpretation based on compositional profiles ambiguous.

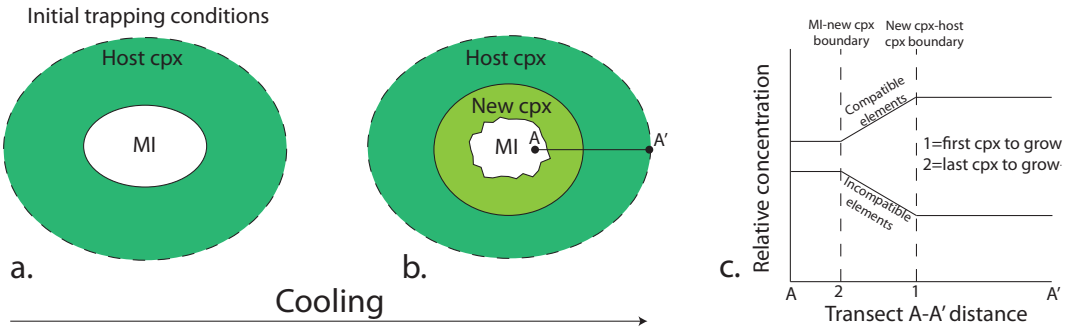

Figure S1. The evolution of post-entrapment crystallization (PEC) and a model for hypothetical chemical gradients. (a) Conditions of initial trapping of MI prior to any PEC. The MI has a rounded shape. (b) As cooling proceeds, the MI begins to react with the host clinopyroxene and precipitate a compositionally distinct clinopyroxene directly from the melt, resulting in changes in the chemistry of the MI and will also leave behind distinct chemical gradients between the MI and the newly-crystallized clinopyroxene (gradients shown in panel c). A chemical profile along the A-A' line should reveal these gradients if diffusion has not been an important process in modifying them. (c) Schematic representation of the predicted behavior of chemical gradients from the MI edge through the host clinopyroxene. The location of the A-A' transect can be seen in panel (b) and is represented on the x-axis of panel (c). Relative concentrations of incompatible and compatible elements are represented on the y-axis. Locations 1 and 2 correspond to the boundary between the MI and newly-crystallized clinopyroxene and original host clinopyroxene, respectively. The compatible elements should show a trend of increasing relative concentrations between the edge of the MI and the host clinopyroxene while the incompatible elements should show the opposite trend. These gradients are not confirmed in the data (see Supporting Figures S2-S9), indicating that PEC processes are not important in the petrogenetic evolution of these inclusions (i.e., the compositions of the inclusions are quite close to the compositions of the original trapped melts).

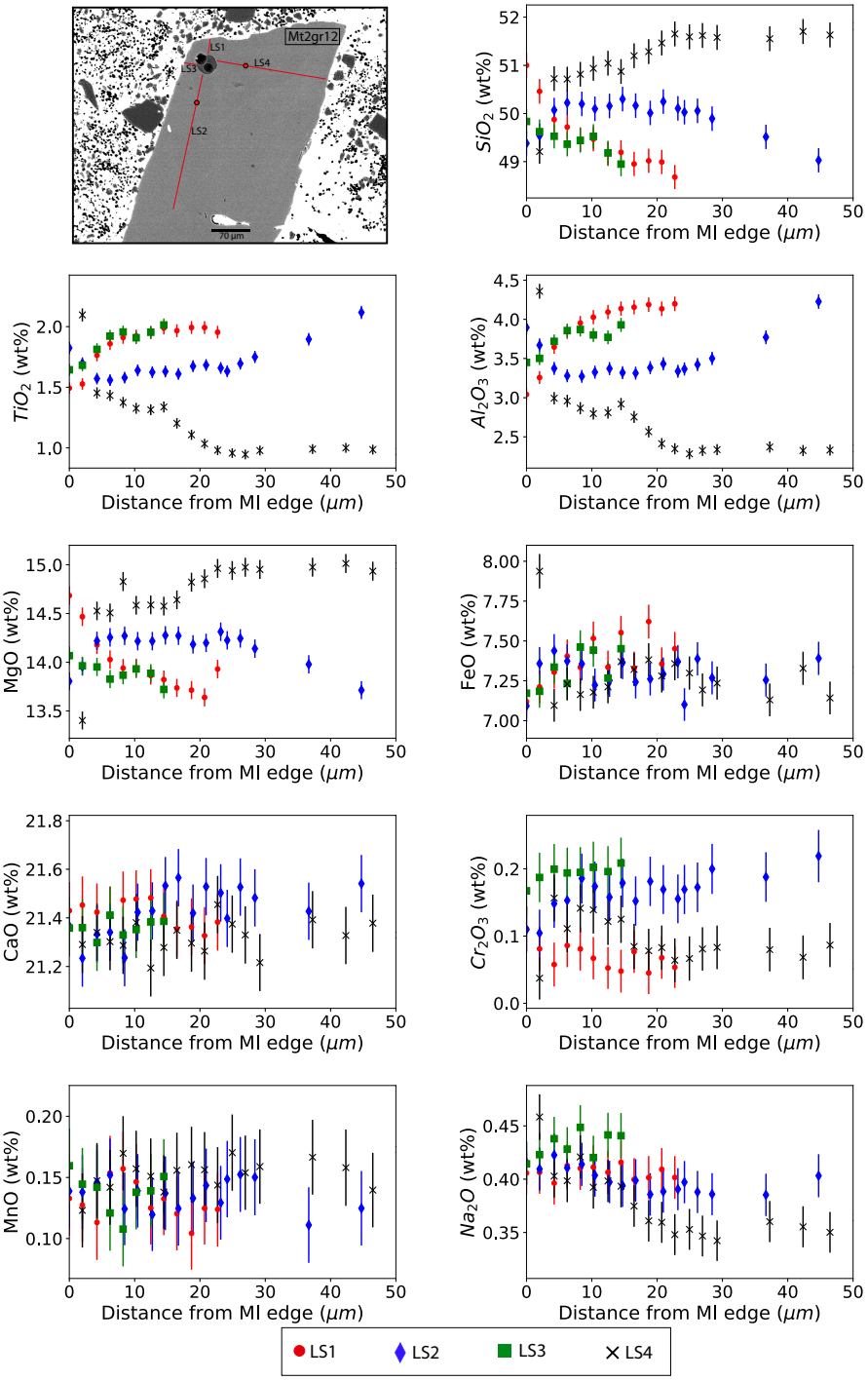

Figure S2: Major element transects through the mt2gr12 host clinopyroxene (the mt2gr12 melt inclusion was also analyzed in this study for major and trace elements). The transects, termed line segments (LS) 1 through 4, are shown in the BSE image (1st panel) of the clinopyroxene where each red line denotes the full extent of each line segment in which data is reported in Supporting Dataset S3, however, only the first 50 µm of each transect is plotted here to better see trends near the MI-clinopyroxene boundary. Each line segment extends from the MI edge out into the clinopyroxene grain where a red circle outlined in black denotes the 50 µm point along the transect. Major element data was collected via EPMA using a 2 µm spot size and error bars are 2σ standard deviation (SD).

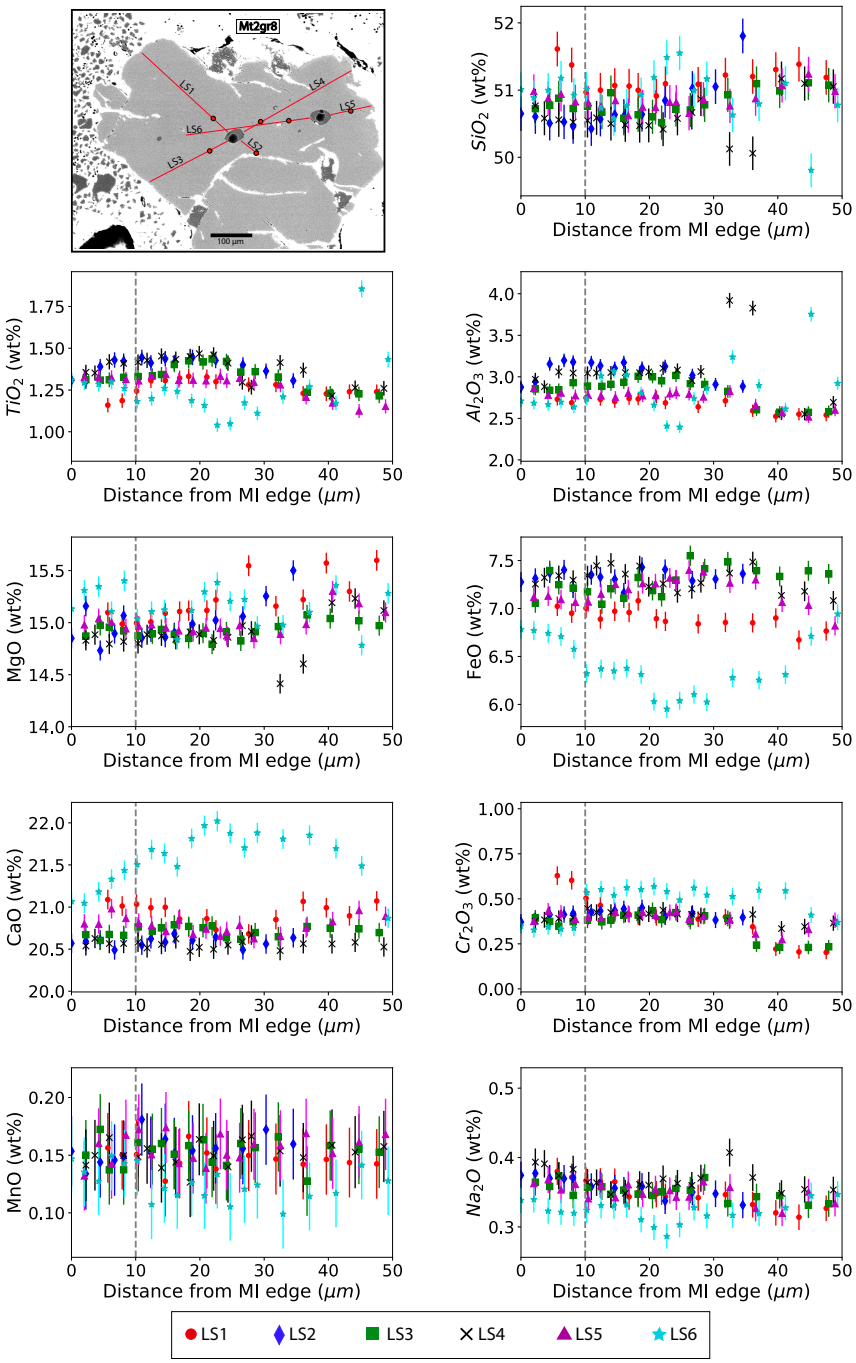

Figure S3. Major element transects through the mt2gr8 host clinopyroxene (the mt2gr8b MI was analyzed for major and trace elements in this study as denoted in the BSE image). The transects, termed line segments (LS) 1 through 6, are shown in the BSE image (1st panel) of the clinopyroxene each red line denotes the full extent of each line segment in which data is reported in Supporting Dataset S3, however, only the first 50 µm of each transect is plotted here to better see trends near the MI-clinopyroxene boundary. Each line segment extends from the MI edge out into the clinopyroxene grain where a red circle outlined in black denotes the 50 µm point along the transect. Major element data was collected via EPMA using a 2 µm spot size and error bars are 2σ SD. Some of the data points of LS6 have been removed as they were contaminated in passing by the central melt inclusion. The grey dashed line denotes the average

distance from the MI edge to the edge of the "halo" feature that can be seen around the mt2gr8b MI (see Figure S10h).

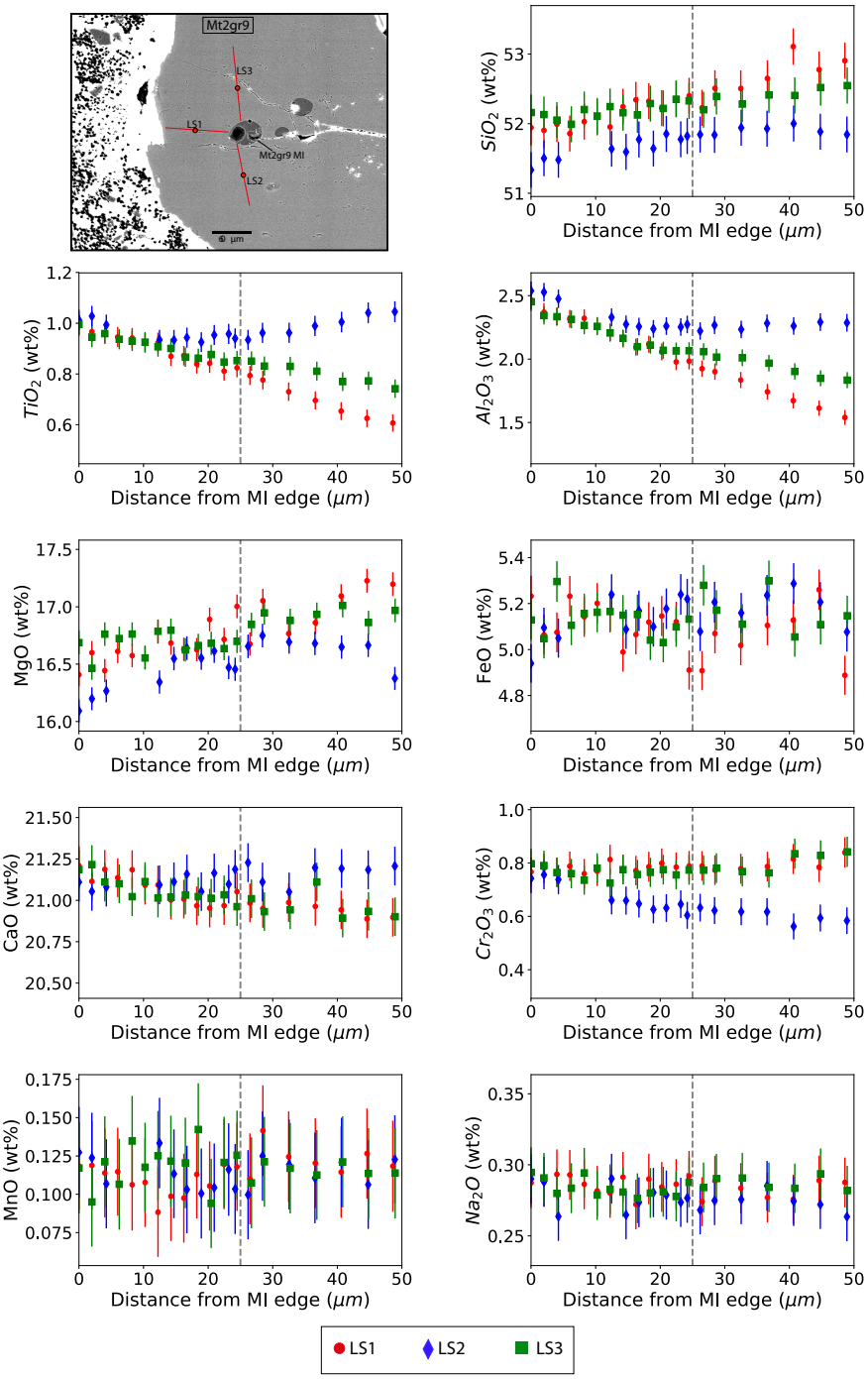

Figure S4. Major element transects through the mt2gr9 host clinopyroxene (the mt2gr9 MI was analyzed for major and trace elements in this study). The transects, termed line segments (LS) 1 through 3, are shown in the BSE image (1st panel) of the clinopyroxene each red line denotes the full extent of each line segment in which data is reported in Supporting Dataset S3, however, only the first 50 µm of each transect is plotted here to better see trends near the MI-clinopyroxene boundary. Each line segment extends from the MI edge out into the clinopyroxene grain where a red circle outlined in black denotes the 50 µm point along the transect. Major element data was collected via EPMA using a 2 µm spot size and error bars are

2σ SD. The grey dashed line denotes the average distance from the MI edge to the edge of the "halo" feature that can be seen around the mt2gr8b MI (see Figure S10i).

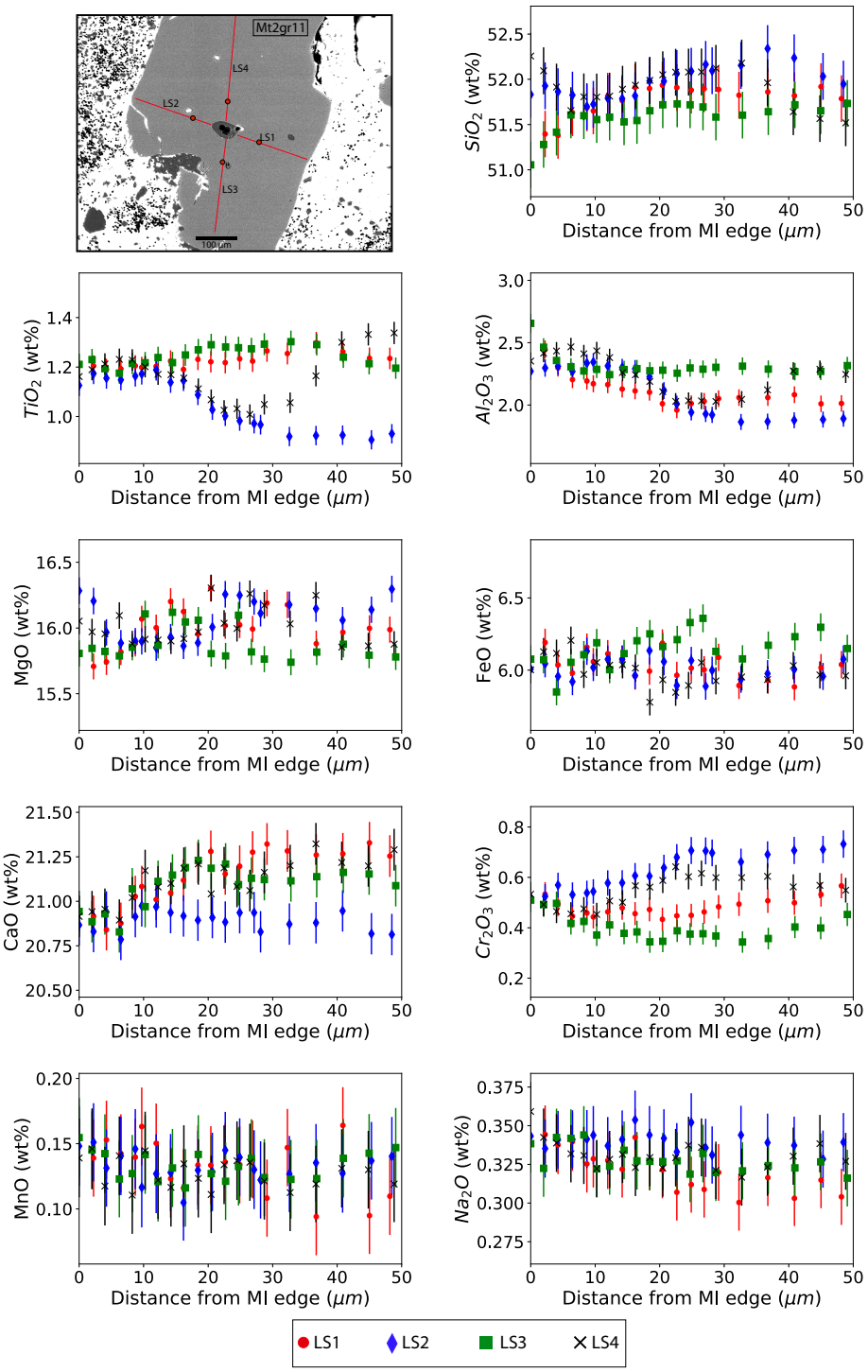

Figure S5. Major element transects through the mt1gr11 host clinopyroxene (the mt1gr11 MI was analyzed for major and trace elements in this study). The transects, termed line segments (LS) 1 through 4, are shown in the BSE image (1st panel) of the clinopyroxene each red line denotes the full extent of each line segment in which data is reported in Supporting Dataset S3, however, only the first 50 µm of each transect is plotted here to better see trends near the MI-clinopyroxene boundary. Each line segment extends from

the MI edge out into the clinopyroxene grain where a red circle outlined in black denotes the 50 µm point along the transect. Major element data was collected via EPMA using a 2 µm spot size and error bars are 2σ SD.

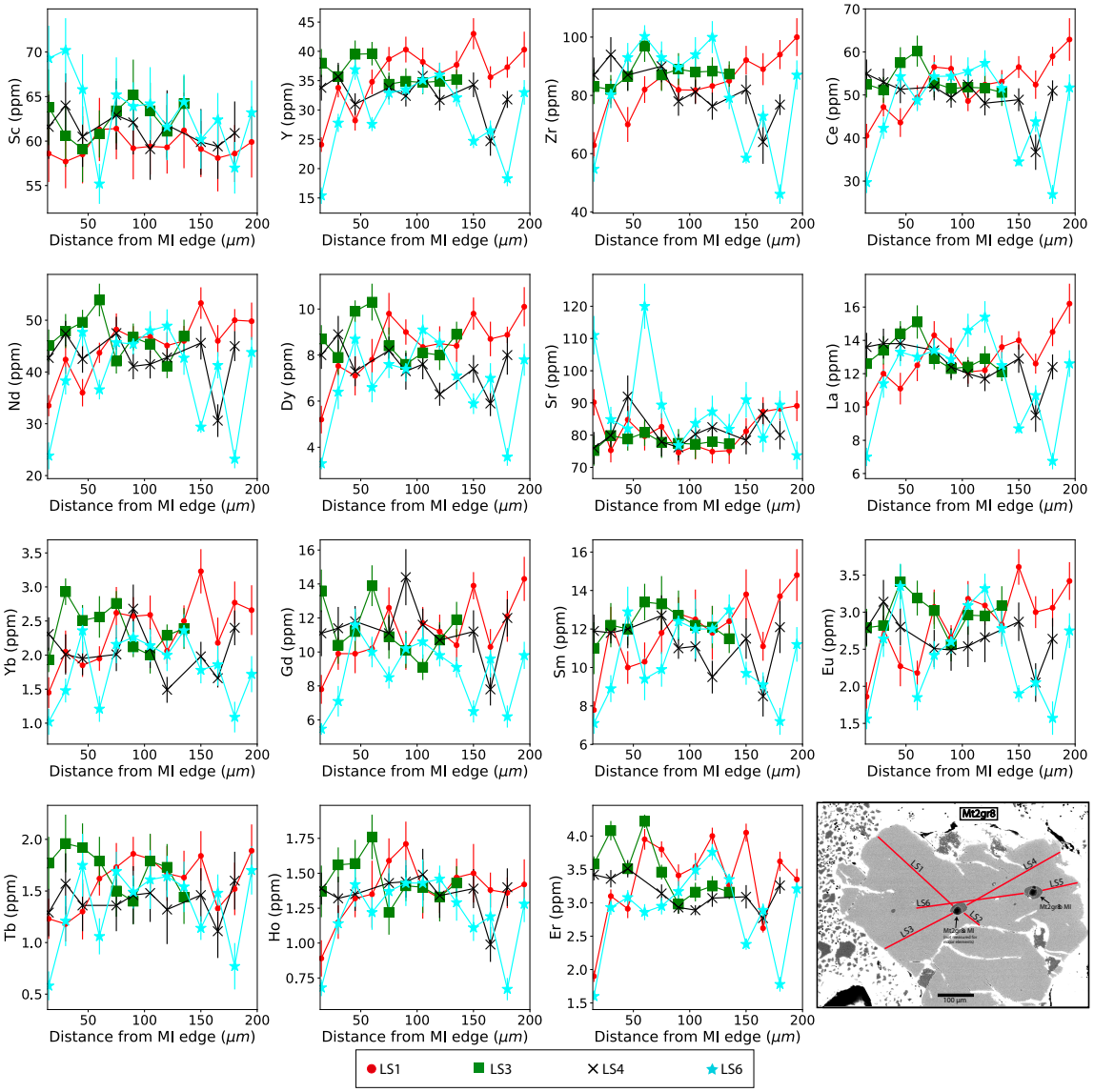

Figure S6: Trace element transects through the mt2gr8 host clinopyroxene (the mt2gr8b MI was analyzed for major and trace elements in this study, as denoted in the BSE image in the last panel). The transects, termed line segments (LS) 1 through 6, are shown in the BSE image (last panel) of the clinopyroxene where each red line denotes the extent of each line segment that can be seen in the trace element plots and is reported in Supporting Dataset S4. Each line segment extends from the MI edge out into the clinopyroxene grain. Trace element data was collected via LA-IC-PMS using a 15 µm spot size and error bars are 2 SE. Trace elements were not measured for each of the line segments that were measured for major elements and therefore that are shown in the BSE image due to space available on the clinopyroxene grain and the large laser spot size.

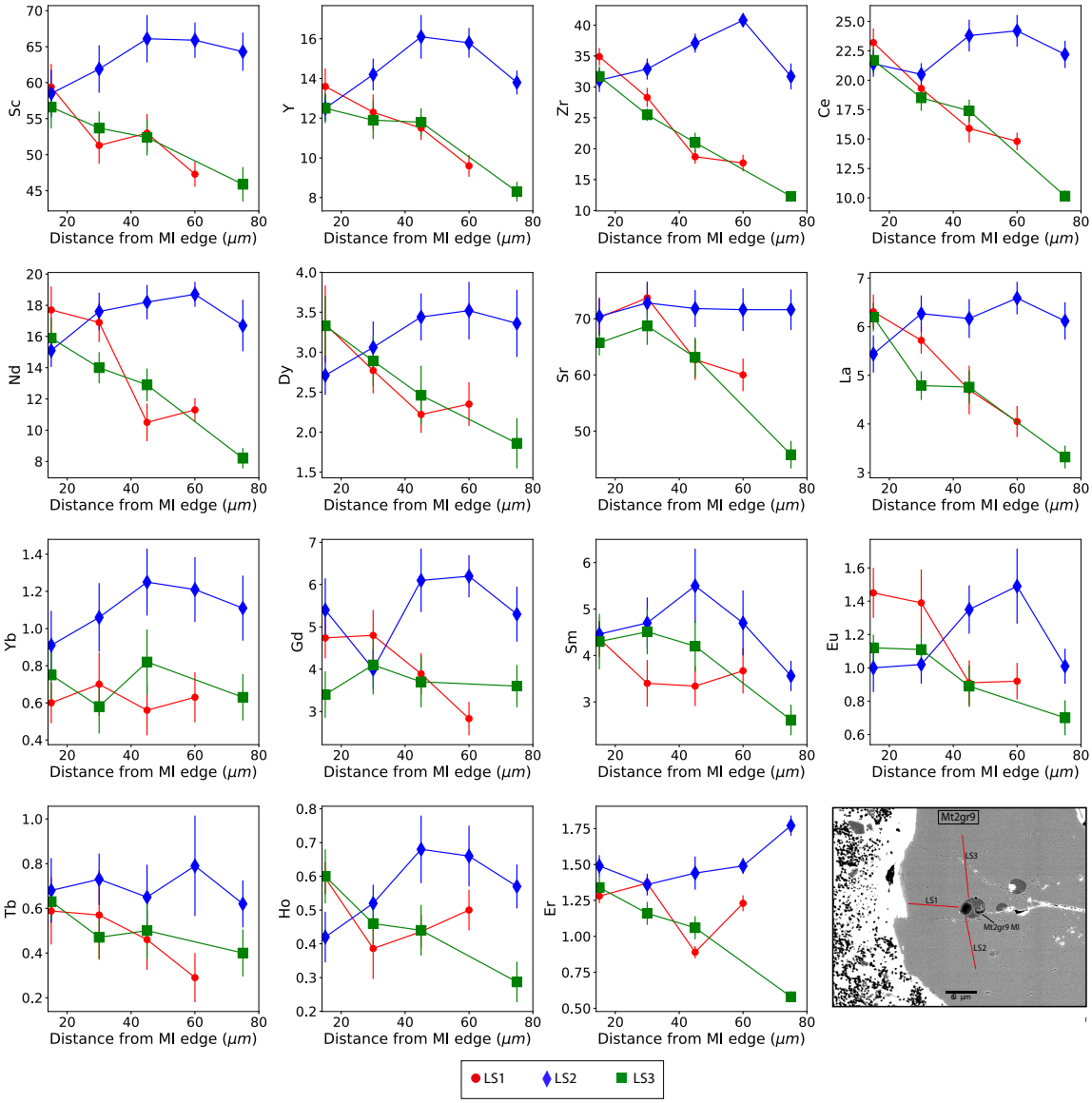

Figure S7. Trace element transects through the mt2gr9 host clinopyroxene (the mt2gr9 MI was analyzed for major and trace elements in this study, and can be seen in the BSE image in the last panel). The transects, termed line segments (LS) 1 through 3, are shown in the BSE image (last panel) of the clinopyroxene where each red line denotes the extent of each line segment that can be seen in the trace element plots and is reported in Supporting Dataset S4. Each line segment extends from the MI edge out into the clinopyroxene grain. Trace element data was collected via LA-IC-PMS using a 15 µm spot size and error bars are 2 SE.

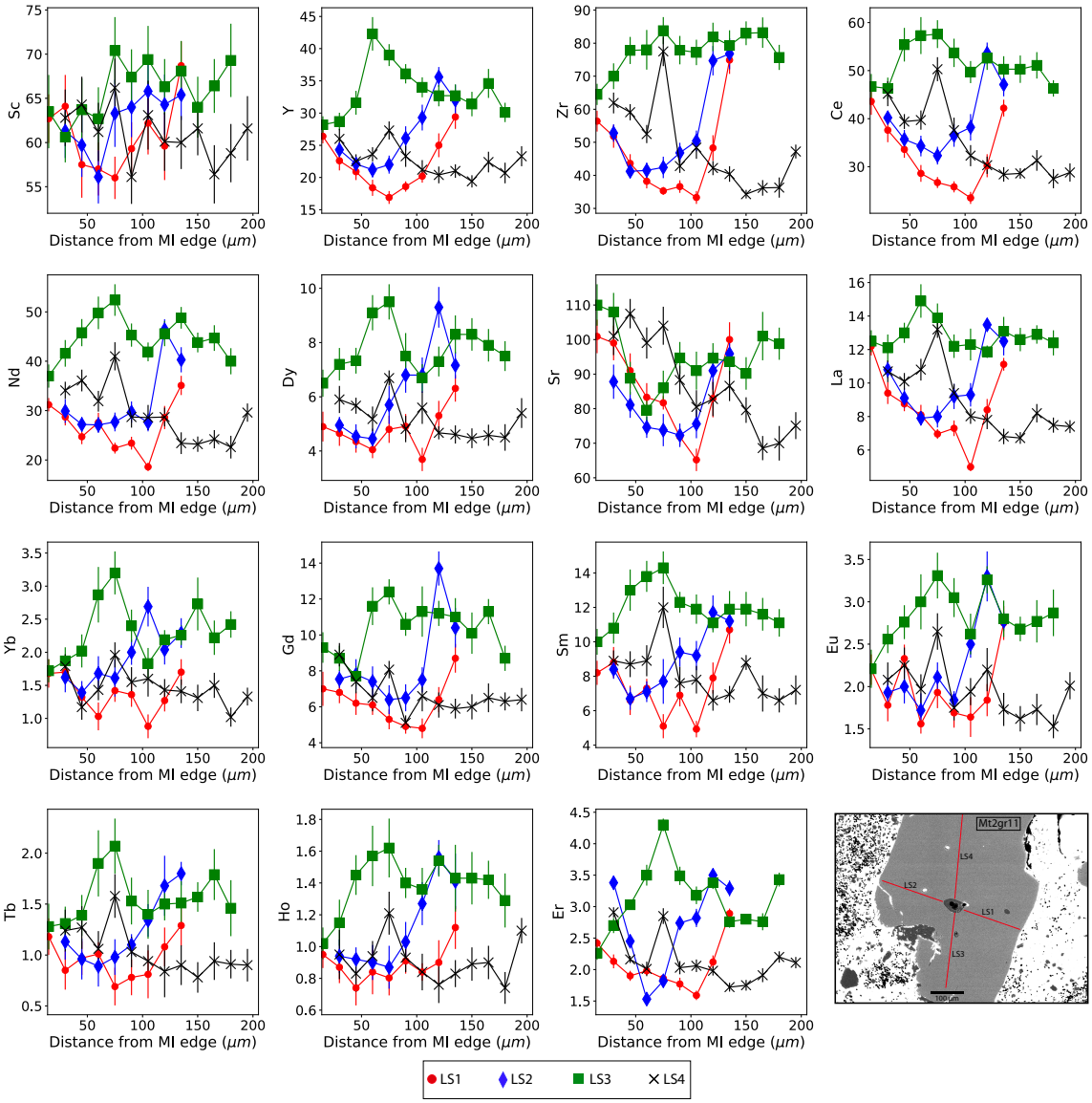

Figure S8 Trace element transects through the mt1gr11 host clinopyroxene (the mt1gr11 MI was analyzed for major and trace elements in this study, and can be seen in the BSE image in the last panel). The transects, termed line segments (LS) 1 through 4, are shown in the BSE image (last panel) of the clinopyroxene where each red line denotes the extent of each line segment that can be seen in the trace element plots and is reported in Supporting Dataset S4. Each line segment extends from the MI edge out into the clinopyroxene grain. Trace element data was collected via LA-IC-PMS using a 15 µm spot size and error bars are 2 SE.

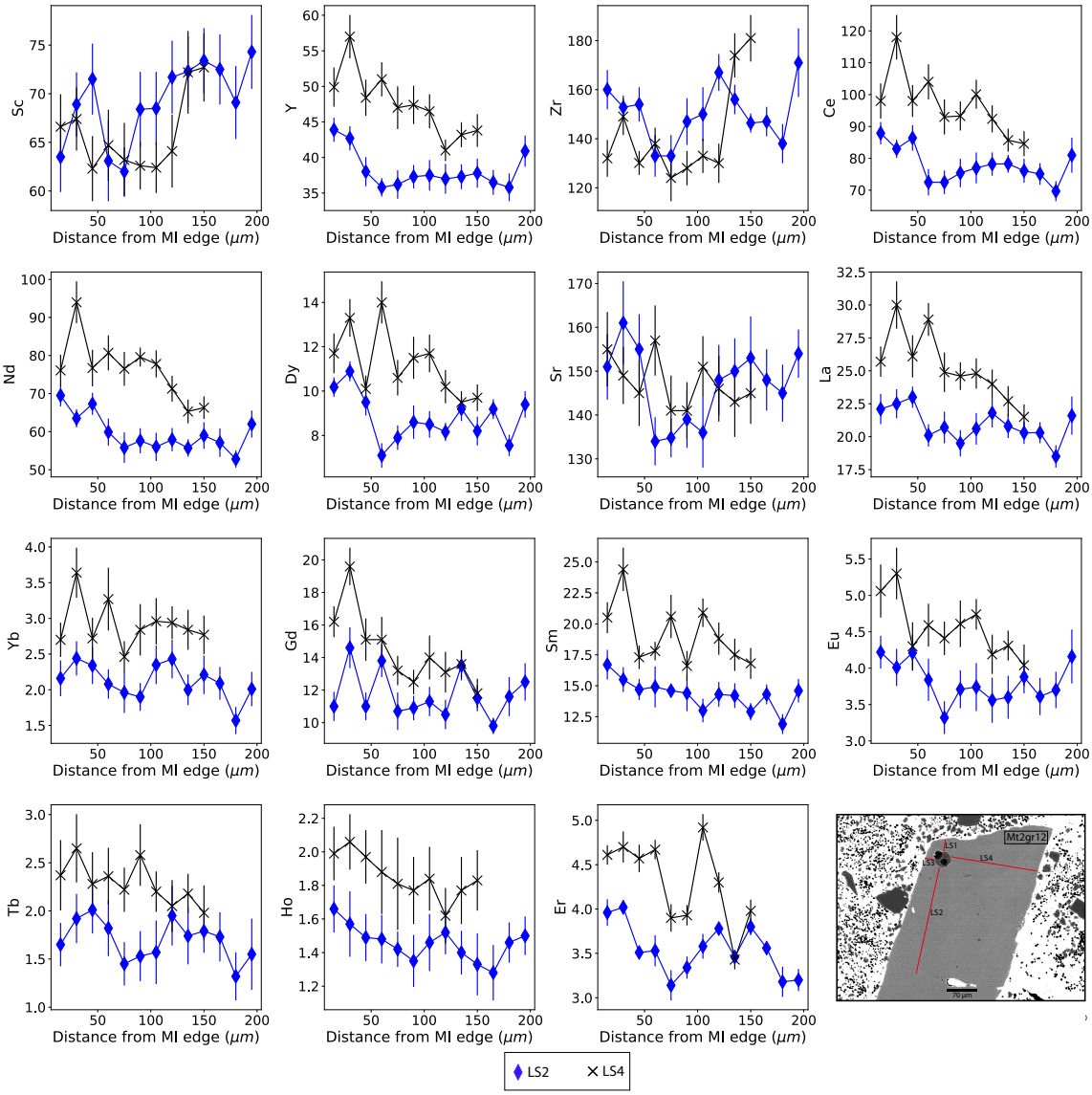

Figure S9. Trace element transects through the mt2gr12 host clinopyroxene (the mt2gr12 MI was analyzed for major and trace elements in this study, and can be seen in the BSE image in the last panel). The transects, termed line segments (LS) 2 and 4, are shown in the BSE image (last panel) of the clinopyroxene where each red line denotes the extent of each line segment that can be seen in the trace element plots and is reported in Supporting Dataset S4. Each line segment extends from the MI edge out into the clinopyroxene grain. Trace element data was collected via LA-IC-PMS using a 15 µm spot size and error bars are 2 SE. Trace elements were not measured for two of the line segments shown in the BSE image due to the laser spot size being too large to analyze the small space available on the clinopyroxene grain for these segments.

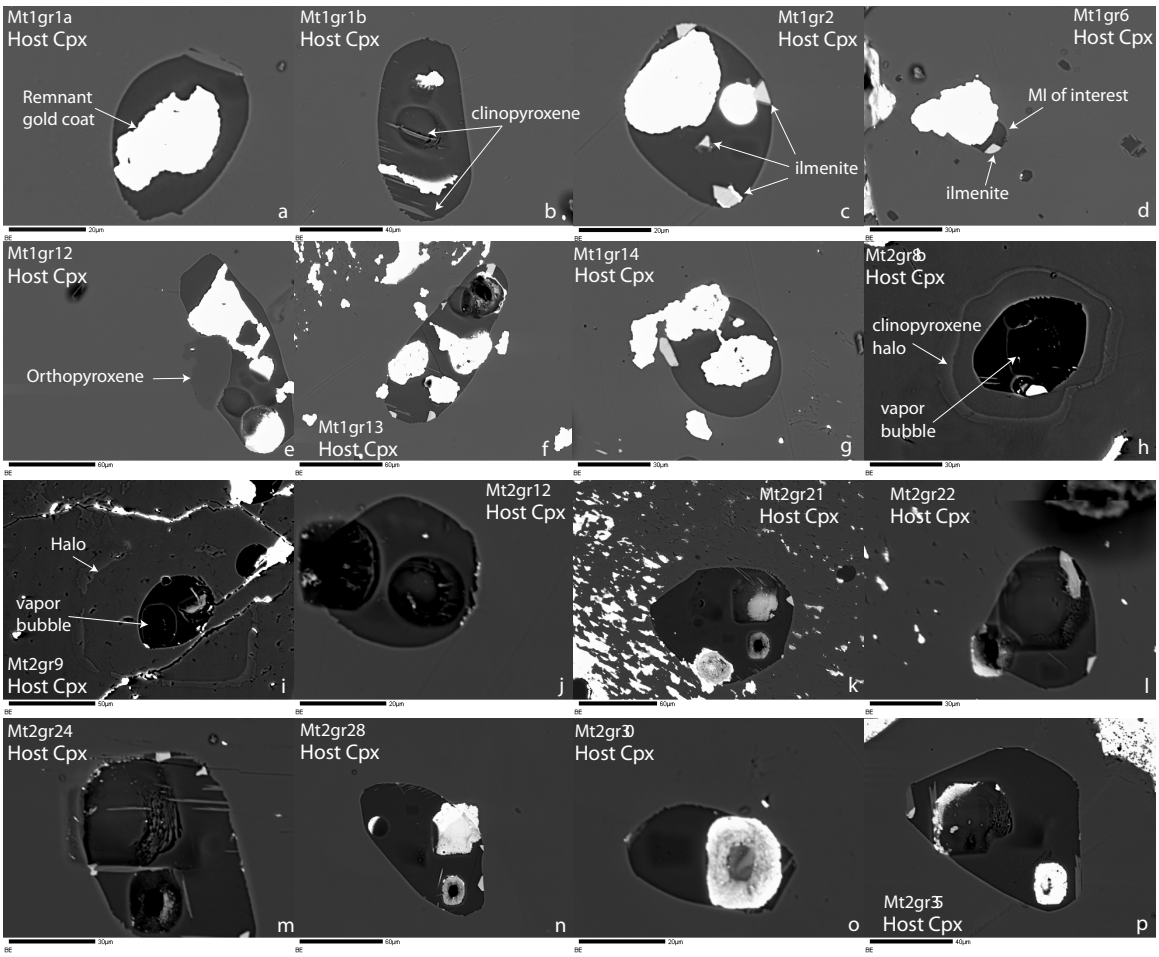

Figure S10. Melt inclusion back-scatter electron images of those melt inclusions *not presented in the main text*. Many inclusions show bright white splotches that is gold coat that was not completely removed prior to imaging (see panel a for example). Due to the delicate nature of these inclusions and their size, care was taken during polishing to remove very little melt inclusion material, thus some gold coat was left behind. The pitted features are ion probe or laser ablation spot analyses. Panels h and i show the two melt inclusions exhibiting the "halo" feature, as described in the text, and additionally are the two melt inclusions with vapor phases. The cracks seen in panel i occurred during sample preparation. Panel e shows the clinopyroxene-melt inclusion pair that contains the only orthopyroxene observed in these samples. Panels a, b, f, k, m, and p show needle-like clinopyroxene crystallization (see labeled example in panel b). Panels c, d, g, l, m, n, and p, show variable amounts of ilmenite crystals (see labeled example in panel c).

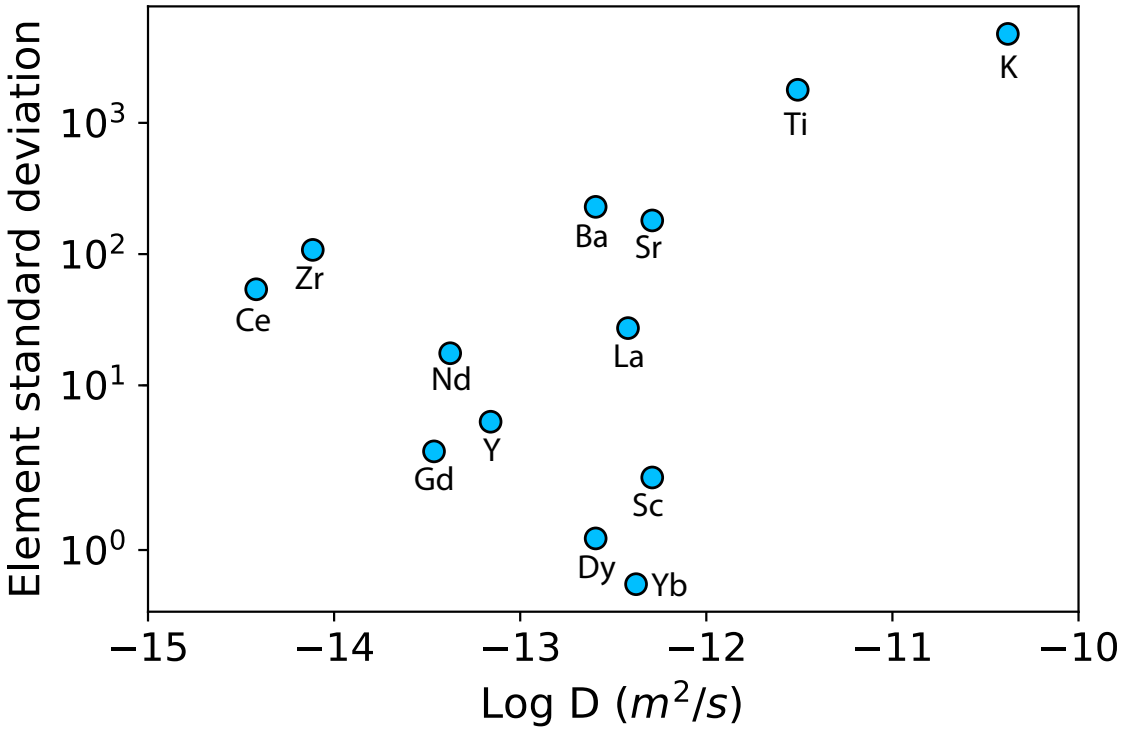

Figure S11: Diffusivity vs trace element standard deviation. Log diffusivities for a trachytic melt at 1150 °C are from Cherniak & Dimanov (2010) and references therein. When diffusivities are plotted against their respective element concentration standard deviation (i.e., 1 standard deviation calculated using all of the melt inclusions for each element indicated on the plot beneath the data points), a correlation should be seen if diffusion has played a role in controlling MI element variability (i.e., faster diffusing elements should show little variation and the slowest diffusing elements should show the most variability). If such a correlation is seen, diffusion has played a minor role in re-distributing and modifying MI trace element chemistry (Michael et al., 2002; Kent, 2008). The element used here are Ce (slowest diffusing element of the group), Sc, Y, Zr, Ba, , Nd, Dy, Sr, La, Yb, Gd, Ti, and K (fastest diffusing element of the group).

Dataset S1. Trace element analysis of ALV 519-4-1 as a secondary standard made during trace element analyses of melt inclusions.

Dataset S2. Major and trace element analyses of clinopyroxene-hosted melt inclusions, host clinopyroxenes, and mt1gr11 crystal inclusions

Dataset S3. LA-ICP-MS 2RSD for the NIST612 reference material used in clinopyroxene trace element analyses.

Dataset S4. EPMA major element analyses of line transects through clinopyroxenes hosting melt inclusions.

Dataset S5. LA-ICP-MS trace element analyses of line transects through clinopyroxenes hosting melt inclusions.

Dataset S6. Major and trace elements of the reconstructed melt inclusion compositions.